Histopathological Image Analysis: A Review

Metin N. Gurcan [Senior Member, IEEE],
Department of Biomedical Informatics, The Ohio State University, Columbus, OH 43210 USA
(phone: 614-292-1084; fax: 614-688-6600; metin.gurcan@osumc.edu).

Laura Boucheron [Member, IEEE],
New Mexico State University, Klipsch School of Electrical and Computer Engineering, Las
Cruces, NM 88003, USA (lboucher@nmsu.edu).

Ali Can [Member, IEEE],
Global Research Center, General Electric Corporation, Niskayuna, NY 12309, USA
(can@research.ge.com).

Anant Madabhushi [Member, IEEE],
Biomedical Engineering Department, Rutgers University, Piscataway, NJ 08854, USA
(anantm@rci.rutgers.edu).

Nasir Rajpoot, and
Department of Computer Science, University of Warwick, Coventry, CV4 7AL, England
(N.M.Rajpoot@warwick.ac.uk)

Bulent Yener [Senior Member, IEEE]
Computer Science Department, Rensselaer Polytechnic Institute, Troy, NY 12180, USA
(yener@cs.rpi.edu)

Abstract

Over the past decade, dramatic increases in computational power and improvement in image
analysis algorithms have allowed the development of powerful computer-assisted analytical
approaches to radiological data. With the recent advent of whole slide digital scanners, tissue
histopathology slides can now be digitized and stored in digital image form. Consequently,
digitized tissue histopathology has now become amenable to the application of computerized
image analysis and machine learning techniques. Analogous to the role of computer-assisted
diagnosis (CAD) algorithms in medical imaging to complement the opinion of a radiologist, CAD
algorithms have begun to be developed for disease detection, diagnosis, and prognosis prediction
to complement to the opinion of the pathologist. In this paper, we review the recent state of the art
CAD technology for digitized histopathology. This paper also briefly describes the development
and application of novel image analysis technology for a few specific histopathology related
problems being pursued in the United States and Europe.

Keywords

histopathology; image analysis; computer-assisted interpretation; microscopy analysis

I. Introduction and motivation

The widespread use of Computer-assisted diagnosis (CAD) can be traced back to the emergence of digital mammography in the early 1990's [1]. Recently, CAD has become a part of routine clinical detection of breast cancer on mammograms at many screening sites and hospitals [2] in the United States. In fact, CAD has become one of the major research subjects in medical imaging and diagnostic radiology. Given recent advances in high-throughput tissue bank and archiving of digitized histological studies, it is now possible to use histological tissue patterns with computer-aided image analysis to facilitate disease classification. There is also a pressing need for CAD to relieve the workload on pathologists by sieving out obviously benign areas, so that pathologist can focus on the more difficult-to-diagnose suspicious cases. For example, approximately 80% of the 1 million prostate biopsies performed in the US every year are benign; this suggests that prostate pathologists are spending 80% of their time sieving through benign tissue.

Researchers both in the image analysis and pathology fields have recognized the importance of quantitative analysis of pathology images. Since most current pathology diagnosis is based on the subjective (but educated) opinion of pathologists, there is clearly a need for quantitative image-based assessment of digital pathology slides. This quantitative analysis of digital pathology is important not only from a diagnostic perspective, but also in order to understand the underlying reasons for a specific diagnosis being rendered (e.g., specific chromatin texture in the cancerous nuclei which may indicate certain genetic abnormalities). In addition, quantitative characterization of pathology imagery is important not only for clinical applications (e.g., to reduce/eliminate inter- and intra-observer variations in diagnosis) but also for research applications (e.g., to understand the biological mechanisms of the disease process).

A large focus of pathological image analysis has been on the automated analysis of cytology imagery. Since cytology imagery often results from the least invasive biopsies (e.g., the cervical Pap smear), they are some of the most commonly encountered imagery for both disease screening and biopsy purposes. Additionally, the characteristics of cytology imagery, namely the presence of isolated cells and cell clusters in the images and the absence of more complicated structures such as glands make it easier to analyze these specimens compared to histopathology. For example, the segmentation of individual cells or nuclei is a relatively easier process in such imagery since most of the cells are inherently separated from each other.

Histopathology slides, on the other hand, provide a more comprehensive view of disease and its effect on tissues, since the preparation process preserves the underlying tissue architecture. As such, some disease characteristics, e.g., lymphocytic infiltration of cancer, may be deduced only from a histopathology image. Additionally, the diagnosis from a histopathology image remains the 'gold standard' in diagnosing considerable number of diseases including almost all types of cancer [3]. The additional structure in these images, while providing a wealth of information, also presents a new set of challenges from an automated image analysis perspective. It is expected that the proper leverage of this spatial information will allow for more specific characterizations of the imagery from a diagnostic perspective. The analysis of histopathology imagery has generally followed directly from techniques used to analyze cytology imagery. In particular, certain characteristics of nuclei are hallmarks of cancerous conditions. Thus, quantitative metrics for cancerous nuclei were developed to appropriately encompass the general observations of the experienced pathologist, and were tested on cytology imagery. These same metrics can also be applied to histopathological imagery, provided histological structures such as cell nuclei, glands, and lymphocytes have been adequately segmented (a complication due to the complex structure

of histopathological imagery). The analysis of the spatial structure of histopathology imagery can be traced back to the works of Wiend *et al*. [4], Bartels [5] and Hamilton [6] but has largely been overlooked perhaps due to the lack of computational resources and the relatively high cost of digital imaging equipment for pathology. However, spatial analysis of histopathology imagery has recently become the backbone of most automated histopathology image analysis techniques. Despite the progress made in this area thus far, this is still a large area of open research due to the variety of imaging methods and disease-specific characteristics.

1.1. Need for Quantitative Image Analysis for Disease Grading

Currently, histopathological tissue analysis by a pathologist represents the only definitive method (a) for confirmation of presence or absence of disease, and (b) disease grading, or the measurement of disease progression. The need for quantitative image analysis in the context of one specific disease (prostate cancer) is described below. Similar conclusions hold for quantitative analysis of other disease imagery.

Higher Gleason scores are given to prostate cancers, which are more aggressive, and the grading scheme is used to predict cancer prognosis and help guide therapy. The Gleason grading system is based solely on architectural patterns; cytological features are not evaluated. The standard schematic diagram created by Gleason and his group (see Figure 1.1) separated architectural features into 1 of 5 histological patterns of decreasing differentiation, pattern 1 being most differentiated and pattern 5 being least differentiated. The second unique feature of Gleason grading is that grade is not based on the highest (least differentiated) pattern within the tumor. Recently several researchers have reported discrepancies with the Gleason grading system for grading prostate cancer histopathology. Many researchers have found grading errors (both under- and over-grading) in prostate cancer studies [7-11]. Similar issues with cancer grading have been reported for other diseases such as breast cancer [12].

In light of the above, Luthringer *et al* [13] have discussed the need for changes to be made to Gleason grading system. In late 2005, the *International Society of Urologic Pathologists* in conjunction with the WHO made a series of recommendations for modifications to the Gleason grading system, including reporting any higher grade cancer, no matter how small quantitatively.

Luthringer *et al*. [13] have also suggested the need for reevaluation of original biopsy material by a highly experienced pathologist which could help guide patient management. Stamey *et al.* [14] discussed need for developing methods to accurately measure cancer volume and better estimate prostate cancer to better predict progression of cancer. King *et al.* [8] has similarly called for developing a methodology to help reduce pathologic interpretation bias which would likely result in significantly improved accuracy of prostate cancer Gleason grading.

1.2. Differences in CAD approaches between radiology and histopathology

While CAD is now being used in radiology in conjunction with a wide range of body regions and a variety of imaging modalities, the preponderant question has been: can CAD enable disease detection? Note that this question, as opposed to more diagnostic questions, is motivated by the inherent limitation in spatial resolution of radiological data. For instance, in mammography, CAD methods have been developed to automatically identify or classify mammographic lesions. In histopathology, on the other hand, simply identifying presence or absence of cancer or even the precise spatial extent of cancer may not hold as much interest as more sophisticated questions such as: what is the grade of cancer? Further, at the

histological (microscopic) scale one can begin to distinguish between different histological subtypes of cancer, which is quite impossible (or at the very least difficult) at the coarser radiological scale.

It is fair to say that since CAD in histopathology is still evolving, the questions that researchers have started to ask of pathology data are not as well articulated as some of the problems being investigated in radiology. A possible reason for this is that image analysis scientists are still trying to come to terms with the enormous density of data that histopathology holds compared to radiology. For instance, the largest radiological datasets obtained on a routine basis are high resolution chest CT scans comprising approximately $512 \times 512 \times 512$ spatial elements or ~ 134 million voxels. A single core of prostate biopsy tissue digitized at 40x resolution is approximately $15,000 \times 15,000$ elements or ~ 225 million pixels. To put this in context, a single prostate biopsy procedure can comprise anywhere between 12-20 biopsy samples or approximately 2.5 – 4 billion pixels of data generated per patient study. Due to their relatively large size and the content, these images frequently need to be processed in a multi-resolution framework.

Also, while radiological CAD systems mostly deal with gray-scale images, histological CAD systems often need to process color images. Furthermore, with the recent advent of multi-spectral and hyper-spectral imaging, each pixel in a histopathology section could potentially be associated with several hundred sub-bands and wavelengths.

These fundamental differences in radiology and histopathology data have resulted in specialized CAD schemes for histopathology. While several similar reviews have been published for CAD in medical imaging and diagnostic radiology [15-23], to the best of our knowledge no related review has been undertaken for digitized histopathology imagery. A survey for CAD histopathology is particularly relevant given that the approaches and questions being asked of histological data are different from radiological data. The motivation of this paper is to present a comprehensive review of the state-of-the-art CAD methods and the techniques employed for automated image analysis of digitized histopathology imagery.

1.5 Organization of this Paper

We have organized this paper to follow the general image analysis procedures for histopathology imagery. These analysis procedures are generally applicable to all imaging modalities. In Section 2, we describe digital pathology imaging modalities including immunofluorescence and spectral imaging and explain the difference between cytopathology and histopathology. In Section 3, image preprocessing steps such as color normalization and tissue autofluorescence compensation are reviewed. In Section 4, we discuss recent advances in detection and segmentation in histopathological images. Section 5 is dedicated to feature extraction and selection at different levels, with real-world examples. In Section 6, we review classification and subcellular quantification. Finally, in Section 7 we discuss some of the potential issues that image analysis of histopathology could be used to address in the future and possible directions for the field in general.

While there are a large number of applicable methods for preprocessing (Section 3), detection and segmentation (Section 4), feature extraction and selection (Section 5), and classification and subcellular quantification (Section 6), we will present here only some common examples. We refer the interested reader to the references contained within the various sections for further reading.

II. Digital pathology imaging modalities

2.1 Histopathology and Cytopathology

Histopathology is the study of the signs of the disease using the microscopic examination of a biopsy or surgical specimen that is processed and fixed onto glass slides. To visualize different components of the tissue under a microscope, the sections are dyed with one or more stains. The aim of staining is to reveal cellular components; counter-stains are used to provide contrast. Hematoxylin-Eosin (H&E) staining has been used by pathologists for over a hundred years. Hematoxylin stains cell nuclei blue, while Eosin stains cytoplasm and connective tissue pink. Due to the long history of H&E, well-established methods, and a tremendous amount of data and publications, there is a strong belief among many pathologists that H&E will continue to be the common practice over the next 50 years [24].

Cytology, on the other hand, is related to the study of cells in terms of structure, function and chemistry. Resulting from the least invasive biopsies (e.g., the cervical Pap smear), cytology imagery is the most commonly encountered for both disease screening and biopsy purposes. Additionally, the characteristics of cytology imagery, namely the presence of isolated cells and cell clusters in the images, and the absence of more complicated structures such as glands make it easier to analyze these specimens compared to histopathology.

2.2 Immuno-fluorecence imaging and multiple imaging modalities

Recently, immuno-fluorescent labeling-based image analysis algorithms have been presented to quantify localization of proteins in tissue [25-27]. Commonly used molecular markers are based on chromogenic dyes (such as DAB), or fluorescent dyes (such as Cy dyes or Alexa dyes). Fluorescent dyes have the advantage of multiplexing the dyes to acquire images of multiple proteins. A general overview of molecular labeling, high throughput imaging, and pattern recognition techniques is presented by Price et al. [28].

With current imaging techniques, it is not possible to simultaneously image H&E dyes and immuno-fluorescent molecular biomarkers due to fluorescent characteristics of the H&E dyes, and due to chemical interactions of H&E dyes with the fluorescently labeled antibodies. Recently, methods have been developed to facilitate sequential imaging and registration techniques that enable different modalities presented digitally from the same histological tissue section. Additionally, sequential imaging and registration enables imaging of multiple immuno-fluorescent stains acquired in multiple steps rather than conventional simultaneous multiplexing techniques. This allows an order of magnitude increase in the number of molecular markers to be imaged for the same tissue section. These techniques make it possible to explore un-examined relationships between morphology, subcellular spatial distribution of proteins, and protein-protein interactions. An example of these techniques is shown in Figure 2.1. For brightfield images, hematoxylin stains the nuclei blue (Figure 2.1a), and for fluorescent images DAPI can be used to stain nuclei (blue channel in Figure 2.1a). The first nuclei image is set as the reference image and each of the subsequent nuclei images are registered to the reference. Once the transformation parameters are estimated, then all the channels at a sequential step are mapped onto the reference coordinate system. Figures 2.3b-d show superimposed b-catenin, pan-keratin and smooth muscle a-actin markers superimposed on the H&E with green pseudo-color [29]. Another recently developed sequential imaging method known as MELC [30] has the ability to produce images of the same specimen with up to 100 proteins by utilizing the photo-bleaching characteristics of the fluorescent dyes.

One of the major problems with such '*multi-channel*' imaging methods is the registration of the multiplexed images, since physical displacements can easily occur during sequential imaging of the same specimen. In [29], the authors used mutual information based error

metrics to register the nuclei images from sequential staining steps. While the fluorescent images include dedicated nuclei channels (such as DAPI), the nuclei images from the H&E images can be computed using decomposition techniques [31,32], or using simple ratio or differencing methods that utilize the fact that blue wavelengths are absorbed less than green and red channels by the hematoxylin dye.

2.3 Spectroscopic Imaging Modalities for Histopathology

In recent years, several spectral data acquisition methods have been employed to aid the diagnosis process with additional information about the biochemical makeup of cells and other tissue constituents. Generally, computerized histopathology image analysis takes as its input a 3-channel (red, green and blue or RGB) color image captured by digital imaging equipment (normally a CCD camera) and attempts to emulate the manual analysis and/or provide additional quantitative information to aid in the diagnosis. While analysis of ordinary color images has been shown to be useful, one of the major drawbacks is that only three color channels of the light spectrum are used, potentially limiting the amount of information required for characterizing different kinds of tissue constituents. On the other hand, recently proposed immuno-histochemistry (IHC) methods are not sufficiently well developed for their use in quantitative pathology [33].

Spectral methods offer a relatively inexpensive way of providing a deeper insight into tissue composition. Most of these methods can be categorized into three broad classes: point spectroscopy, spectral imaging, and spectroscopic imaging. *Point spectroscopy* is a well-established area of study whereby, in the context of histopathology, the chemical composition of a tissue sample is ascertained with the help of the spectrum emitted or absorbed at a specific point on the biopsy. Point spectroscopy methods can employ both visible light and beyond. *Spectral imaging,* also known as multi-spectral or hyper-spectral imaging, measures intensity of light from the entire optical field after exciting the sample with visible light of varying wavelengths. *Spectroscopic imaging* combines the strengths of both of the above two methods, building spatial imaging of the human tissue in a multitude of wavelength regimes.

2.3.1 Point Spectroscopy—Vibrational spectroscopy is the most widely researched point spectroscopy method for characterization of normal and diseased tissue. It measures molecular vibrations, induced by incident light, corresponding to the chemical makeup at the molecular level in two different ways: absorption of electromagnetic radiation or frequency shifts between incident and scattered light – the so-called *Raman scattering* effect.

In case of infrared (IR) absorption spectroscopy, the sample is irradiated with a mid-IR beam and the transmitted light is examined for absorption of energy. The *absorption spectrum*, a plot of absorption versus different wavelengths, can reveal the biochemical makeup of the molecules. IR spectroscopy has been used to analyze tissue constituents at a molecular level for almost 60 years [34,35]. Indeed, IR spectra was investigated for characterization of normal and neoplastic tissue as far back as 1952 by Woernley [36], who also showed that the absorption at certain frequencies can be correlated with the concentrations of nucleic acids in tissues. Recent advances in machine learning and pattern recognition algorithms and the development of the IR spectroscopic imaging modality have renewed interest in this technique for studying the biochemical makeup of healthy and diseased tissue.

In Raman spectroscopy, the sample is illuminated with a monochromatic visible or near-IR (NIR) light from a laser source and frequency shifts in the scattered light are measured. The *Raman spectrum* is a plot of intensity of the scattered photon versus shifts in its frequency, often measured in terms of wave numbers in cm^{-1}. NIR-Raman spectroscopy is often used

as an alternative to IR spectroscopy since NIR light has higher energy than mid-IR light and can penetrate much farther into the sample.

Fourier-transform (FT) spectroscopy, known as FT-IR when IR light is used, allows a faster acquisition of the IR spectra by using an interferometer followed by the Fourier transform (FT). FT-IR spectroscopy is the most commonly used form of IR spectroscopy.

2.3.2 Spectral Imaging—Spectral imaging is carried out by building an image cube with slices corresponding to images of the same scene obtained by incident light at differing wavelengths. This technique is referred to as multi-spectral (MS) or hyper-spectral (HS) imaging depending on the number N_b of spectral bands, individual slices of the image cube in the spectral direction (generally with $N_b \leq 40$ for MS and $N_b > 40$ for HS).

2.3.3 Spectroscopic Imaging—Spectroscopic imaging is similar to spectral imaging in that a volumetric cube is obtained with a spectrum per pixel in the optical field. The main difference is that spectroscopic imaging builds the image cube by dividing the image scene into a uniform Cartesian grid, raster scanning the scene according to the grid, and collecting point spectra for each of the grid points.

Fernandez *et al.* [33] have proposed an IR spectroscopic imaging method based on a Michelson interferometer and all-reflecting microscope equipped with a 16-element linear array detector with a narrow aperture size of $6.25\mu m \times 6.25\mu m$. A massive 1,641-dimensional point spectrum was obtained for each pixel spanning a spectral range of 4,000–$720cm^{-1}$ at an effective spectral resolution of $2cm^{-1}$ and at a spatial resolution of $6.25\mu m$. Tissue sections were also stained with H&E and imaged with a digital light microscope for manual histopathology analysis.

While most of the above methods are generally invasive for internal body organs, magnetic resonance spectroscopy (MRS) is a completely non-invasive way of probing the biochemical makeup of tissue. By this virtue, it is a particularly attractive prospect for the imaging of brain tumors, along with magnetic resonance (MR) imaging which has become a mainstay in the diagnosis of suspicious brain lesions [37]. The main principle behind MRS imaging is the *chemical shift* process, the process whereby different *metabolites* in the tissue respond at different resonating frequencies, with the chemical shift often measured in parts per million (ppm). One particular advantage of MRS is that it can be tuned to specific nuclei in the tissue; with hydrogen (^{1}H, also known as proton) being the most commonly studied one. Studies have shown clear differences between ^{1}H MRS spectra of brain tumors and normal brain [38].

2.3.4. Spectral Analysis for Histopathology—In IR spectroscopy, McIntosh *et al.* [39] investigated the use of infrared spectroscopy for the characterization of *in vitro* basal cell carcinoma (BCC) specimens, exploiting the fact that mid-IR light is absorbed by a variety of skin components. Point spectroscopy was performed using an IR spectrometer and an aperture of $20\mu m \times 20\mu m$ from carefully selected regions containing only one type of skin lesion. Their analysis of the normalized spectra employing linear discriminant analysis (LDA) identified absorption bands that arise mainly from CH2 and CH3 absorptions in dermal spectra that are similar to those seen in samples rich in protein and collagen in particular. H&E staining for standard histological examination was carried out after the spectra had been obtained. In a more recent paper, McIntosh *et al.* [40] utilized LDA to analyze the near-IR (NIR) absorption spectrum for non-invasive, *in vivo* characterization of skin neoplasms. Their rationale for using NIR light was that the mid-IR light could be completely absorbed by samples greater than 10–$15\mu m$ in thickness, therefore limiting the utility of mid-IR spectroscopy to *in vitro* analysis.

In Raman spectroscopy, Frank *et al.* [41] examined Raman spectra from breast and observed that visible laser excitation could be used to reveal Raman features for lipids and carotenoids. Huang *et al.* [42] explored the use of a rapid acquisition NIR Raman spectroscopy system for *in vitro* diagnosis of lung cancer. Student's *t*-test was performed to discriminate between normal and malignant bronchial tissues using the ratio of Raman intensity at two specific wavelengths. Chowdary *et al.* [43] showed that the Raman spectra could be useful for discriminating between normal and diseased breast tissues, although a simple Principle Component Analysis (PCA) of spectra was employed for discrimination purposes. Analyzing the Raman spectra of malignant breast tissues, they concluded that malignant tissues had an excess of lipids and proteins. Robichaux-Viehoever *et al.* [44] investigated the use of NIR Raman spectra for the detection of cervical dysplasia and achieved high correlation between the results of their spectral analysis and the histopathology diagnosis.

Recently, Wang *et al.* [45] have shown that FT-IR spectroscopy can be effectively used for detecting pre-malignant (dysplastic) mucosa and leads to better inter-observer agreement, in terms of the κ-statistic. Oliveira *et al.* [46] have explored a setup involving a fixed-wavelength (1064*nm*) laser line as an excitation source and FT-Raman for generating the spectra. Spectral analysis using principal component analysis (PCA) and Mahalanobis distance were used to detect dysplastic and malignant oral lesions. Their results using LDA showed effective separation of spectra of benign lesions from those of pre-malignant and malignant lesions. Over the years, multi-spectral (MS) and hyper-spectral (HS) imaging have demonstrated an enormous potential in remote-sensing applications, leading many researchers to expect promise about their usefulness in histopathology [47]. This promise has been demonstrated by [48] and [49] in their work on the diagnosis of colon adenocarcinoma. However, two recent studies [50,51] have found that the additional spectral information does not significantly improve the classification results. This may be due to the fact that most MS and HS imaging methods employ the visible part of light spectrum which may not be very useful in terms of highlighting important biochemical characteristics, as opposed to the near-IR or mid-IR spectrum. The number of stains present in the sample, as well as the characteristics of the stains themselves will also directly affect the performance of MS and HS image analysis methods.

In MR Spectroscopy, several studies, such as [52], can be found in the literature that report high correlation between automatic grading of *in vivo* tumors and their corresponding post-operative histopathology findings. However, MRS spectral analysis has traditionally been limited to rather simplistic ratio tests. Tiwari *et al.* [53] recently proposed an unsupervised spectral clustering based algorithm for diagnosis of prostate cancer from the MRS spectra, reporting higher specificity compared to the popular *z*-score scheme, routinely used for the analysis of MRS data.

Spectral analysis using different modalities discussed above has demonstrated its potential for diagnosis and grading of cancer in tissue samples. However, as outlined above, most of the proposed algorithms in the literature make use of linear subspace projection methods (PCA, LDA etc) for analysis of the spectral data despite the fact that spectral signatures of different types of tissue in the high-dimensional space may not be linearly separable. Furthermore, a few challenges are limiting the success of such methods in the realm of optical diagnostics. These include, but are not limited to, storage and transmission, registration, processing and analysis of large amounts of data generated by spectral data acquisition methods. The problem is further compounded when gathering spectral imaging data for whole slides. However, the availability of powerful computational resources at increasingly low prices and recent advances in image analysis have meant that more sophisticated methods can now be applied for analyzing large amounts of spectral data.

III. Image pre-processing: color and illumination normalization

3.1. Color Normalization

One of the first steps essential for both fluorescent and bright field microscopy image analysis is color and illumination normalization. This process reduces the differences in tissue samples due to variation in staining and scanning conditions. The illumination can be corrected either using calibration targets or estimating the illumination pattern from a series of images by fitting polynomial surfaces [29]. Another approach is to match the histograms of the images. Software that corrects for spectral and spatial illumination variations is becoming a standard package provided by most bright field manufacturers. This is an essential step for algorithms that heavily depend on color space computations. Yang and Foran [54] presented a robust color based segmentation algorithm for histological structures that used image gradients estimated in the *LUV* color space to deal with issues of stain variability. In the next section, we give detailed description of correcting another artifact, tissue autofluorescence, in fluorescent images.

3.2. Compensating for Tissue auto-fluorescence

Tissue auto-fluorescence (AF) is a fundamental problem in microscopy applications, particularly in retrospective studies that use formalin fixed paraffin embedded tissue sections. AF reduces the signal detection sensitivity, and in some cases even causes failure in the detection of fluorescent biomarker signals. In [29] a two-step technique was used to remove the AF from fluorescent microscopy images. Rather than acquiring images of all the dyes at once using a set of optimum filter cubes tuned to specific dyes, the acquisition is done in two steps. In the first step, tissue is stained with only the low AF dyes (e.g. ultra-violet or infra-red), and images are acquired using all the filter cubes. Images of these cubes, except the low AF dyes, represent the tissue AF at their specific spectra. In the second step, all the remaining dyes are added, and images of all the cubes are acquired again. Then the first set of images is aligned with the second set using a transformation estimated by registering the low-AF images that are common in both steps.

The first step before any AF removal is the correction of the excitation light pattern. The observed image, $I(x, y)$ can be modeled as a product of the excitation pattern, and the emission pattern. While the emission pattern captures the tissue dependent fluorescent staining, the excitation pattern captures the excitation light. In the logarithm domain, the multiplicative relation can be transformed into a linear form. The excitation pattern can be estimated using the mean of the brightest set of pixels from an ordered set of N images;

$$E'_{\mathrm{AVE}}(x, y) = \frac{1}{K}\sum_{n=1}^{K} \log\left(I_n(x, y)\right),$$

(3.1)

where $I_n(x, y)$ denote the ordered pixels ($I_1(x, y) \geq I_2(x, y) \geq \mathrm{L}\ I_n(x, y)\ \mathrm{L} \geq I_N(x, y)$) and K represents the set of brightest pixels. Assuming that a certain percentage of the image occupies stained tissue (non-zero backgound), K is set to an integer to represent this percentage (10% in our experiments). This approximation holds if a large number of images are used in the averaging process. However, a large percentage of pixels are already excluded to eliminate the non-tissue pixels in the images. To overcome the limited sampling size, the log of the excitation pattern estimated in equation (3.1) can be approximated with polynomials. The surface generated by the polynomial coefficients are then used to correct individual images [55].

After the images are corrected for their light excitation pattern, the images between the two sequential steps are aligned. From the two common images, one being the reference image from the first step, $F(x, y)$, and the second being from the subsequent step, $S(x, y)$ a rigid transformation $\mathbf{T}_{FS}$ is obtained, such that the image similarity measure, between $F(x, y)$ and $S(\mathbf{T}_{FS}(x, y))$ is maximized,

$$\underset{\mathbf{T}_{FS}}{\arg\max} Similarity \left(F\left(x, y\right), S\left(\mathbf{T}_{FS}\left(x, y\right)\right)\right)$$

(3.2)

Due to its robustness in registering multi modality images, a mutual information based image similarity measure is used to deal with tissue loss and folding. Additional robustness is achieved by incorporating the mutual information estimation in a multi-resolution framework [56].

Once $\mathbf{T}_{FS}$ is estimated, all the channels are transformed with this transformation to represent all the images in both acquisitions in the same coordinate system. Then the first set of images is subtracted from the second set of images. To achieve the highest dynamic range, the first set of AF images can be acquired in longer exposure times than the second set of AF-dye mixture images. Figures 3.1 shows the acquisition of the Cy3 channel before and after the tissue is stained with Cy3 dye directly conjugated with Estrogen Receptor (ER). The tissue is also stained with a low AF ultraviolet nuclear stain, DAPI (not shown in the figure), which is acquired in both steps and used for aligning the images. The AF removed image is shown in Fig 3.1c. The arrows point to successfully removed high-AF regions, such as red blood cells. Removing the AF using the proposed two-step approach enables accurate image analysis and quantitation for low abundance proteins and directly conjugated antibodies.

IV. automated detection and segmentation of histopathology images

One of the pre-requisites to grading or diagnosis of disease in histopathology images is often the identification of certain histological structures such as lymphocytes, cancer nuclei, and glands. The presence, extent, size, shape and other morphological appearance of these structures are important indicators for presence or severity of disease. For instance, the size of the glands in prostate cancer tend to reduce with higher Gleason patterns [57]. Similarly the presence of a large number of lymphocytes in breast cancer histopathology is strongly suggestive of poor disease outcome and survival [58]. Consequently, a pre-requisite to identification and classification of disease is the ability to automatically identify these structures. These approaches can either be global, in which they attempt to simultaneously segment all the structures in the image scene or local approaches which target specific structures.

Another motivation for detecting and segmenting histological structures has to do with the need for counting of objects, generally cells or cell nuclei. Cell counts can have diagnostic significance for some cancerous conditions. Bibbo *et al*. [59] reported 1.1%-4.7% error in cell counts compared to manual counts for Feulgen-stained prostate specimens. Belien *et al*. [60] found 19-42% error in counting mitoses in Feulgen-stained breast tissue sections. In immunohistochemically stained bone marrow biopsies, Markiewicz *et al*. [61] reported 2.8-10.0% difference in counts between manual and automatic methods, while Kim *et al*. [62] found a correlation of 0.98 between manual and automatic counts of immunostained slides of meningiomas. Sont *et al*. [63] found a correlation of 0.98 between automated and semi-automated methods for inflammatory cell counts in immunostained bronchial tissue.

4.1. Local, structural Segmentation

4.1.1 Nuclear Segmentation—Numerous works have been conducted [64-66] on segmentation of various structures in breast histopathology images using methodologies such as thresholding, fuzzy c-means clustering and adaptive thresholding [66]. Thresholding tends to work only on uniform images and does not produce consistent results if there is considerable variability within image sets. Watershed algorithms tend to pose the same problem [65] due to variability in image sets. Active contours are widely used in image segmentation; however, contours enclosing multiple overlapping objects pose a major limitation. In addition, inclusion of other irrelevant objects from the background further complicates the possibility of obtaining a viable segmentation.

The pixel-level analysis of unstained prostate slides by Fourier transform infrared spectroscopy resulted in 94%-100% accuracy in the pixel-level classification of 10 histologic classes as reported by Fernandez *et al*. in [67]. The pixel-level classification of nuclear material by Boucheron *et al*. [68] resulted in performances (equal tradeoff between detection and false alarm rates) of 88-90% for H&E stained breast tissue. The use of automated methods for pixel-level analysis is perhaps more common for immunostained or fluorescently stained specimens. Singh *et al*. [69] reported 98% accuracy in the detection of positive and negative prostate nuclei immunostained for androgen receptor protein expression. Analysis of cytokeratin-stained lymph node sections yielded 95% detection of stained cells as reported by Weaver *et al*. in [70]. However, these studies focus only on finding individual nuclei.

In H&E stained imagery of astrocytomas and bladder tissue, Glotsos *et al*. [71] reported that 94% of nuclei were correctly delineated. Latson *et al*. found 25% poorly segmented nuclei, 4.5%-16.7% clumped nuclei, and 0.4%-1.5% missed nuclei in H&E stained breast biopsies. Fluorescently stained imagery of cervical and prostate carcinomas allowed for 91%-96% accuracy in cell segmentation by Wahlby *et al.* [72], where the accuracy here is calculated based on manual cell counts (i.e., not taking into account the accuracy of the actual nuclear delineation). Korde *et al.* used image intensity thresholding to segment nuclei in the bladder and in skin tissue [73]. Gurcan *et al*. leveraged gray level morphology followed by hysteresis thresholding to achieve cell nuclei segmentation in digitized H&E stained slides [74,75]. Other algorithms have been proposed using more complex techniques, such an active contour scheme for pap-stained cervical cell images by Bamford and Lovell [76] and a fuzzy logic engine proposed by Begelman, *et al.* [77] for prostate tissue that uses both color and shape based constraints.

In [64,78] nuclear segmentation from breast and prostate cancer histopathology was achieved by integrating a Bayesian classifier driven by image color and image texture and a shape-based template matching algorithm (Figure 4.1). Figure 4.1(a) shows a DCIS study with a number of nuclei closely packed together. The likelihood image representing the probability of each pixel corresponding to a nuclear region is shown in Figure 4.1(b). Note that several nuclei lie adjacent to each other and hence template matching is used to extricate the individual nuclei. Figure 4.1(c) shows the result of thresholding the Bayesian likelihood scene (95% confidence level). Template matching is then done at every location in 4.1(c). Only those image locations where correspondence between the binary segmentation (Figure 4.1(c)) and the template was found are shown as bright. The final nuclear boundary detection (green dots) is displayed in Figure 4.1(d). 4.1.2. Gland segmentation: In a recently presented scheme for extracting glandular boundaries from histopathology scenes [64], the algorithm consists of three distinct components: In the first stage a Bayesian classifier is trained based on color and textural information to automatically identify nuclei, cytoplasm, and lumen regions in the scene. This information is used to train a supervised classifier to identify candidate nuclear, cytoplasmic, and lumen regions within the histological scene.

Following low-level Bayesian classification, structural constraints are incorporated to constrain the segmentation by using image Information regarding the specific order of arrangement of glandular structures (central lumen, surrounding cytoplasm and nuclear periphery) in order to reduce number of false positive gland regions. Finally, a shape-based segmentation method in the form of level sets [79] is initialized within candidate lumen regions as determined from the Bayesian classifier. Hence the level set surface evolution is controlled by the Bayesian probability scene derived via use of the low-level image information. The level set evolution is stopped at the interface between lumen and cytoplasm and thus a segmentation of the inner gland boundary is obtained. A second level set is then initialized within the cytoplasm area and used to capture the outer gland margin. Once the possible gland lumens are found, boundary segmentation is performed using level-sets. A boundary B evolving in time t and in the 2D space defined by the grid of pixels C is represented by the zero level set B = {(x, y)|f(t, x, y) = 0} of a level set function f, where x and y are 2D Cartesian coordinates of c Î C. The evolution of f is then described by a level-set formulation adopted from [79]:

$$\frac{\partial \phi}{\partial t} + F|\nabla \phi| = 0$$

(4.1)

where the function F defines the speed of the evolution. The curve evolution is driven by the nuclei likelihood image. The initial contour $\phi_0 = \phi(0, x, y)$ is initialized automatically using the detected lumen area from the candidate gland regions. The curve is evolved outward from the detected lumen regions in the combined nuclei likelihood image to avoid noise and allow smoother evolution relative to the original image. The intensities of the nuclei likelihood image form the stopping gradient. The algorithm is run until the difference in the contours in two consecutive iterations is below an empirically determined threshold. During training, size distributions similar to those used to calculate object likelihood are created using the final contours. These nuclear boundary based distributions are used to remove regions that are too large to be true glands. Finally, the lumen and nuclear boundaries extracted from true gland regions are passed on to the next step for feature extraction. Sample results from the automated gland segmentation algorithm are shown in Figure 4.2. The lumen boundaries are displayed in a solid blue contour and the interior nuclear boundaries are displayed as dashed black lines. Results of our gland segmentation algorithm are shown for sample images from benign epithelium, intermediate, and high-grade prostate cancer (from left to right).

4.2 Global Scene Segmentation Approaches

In [26], a unified segmentation algorithm for subcellular compartmentalization was presented. Quantitation of biomarkers at sub-cellular resolution requires segmentation of sub-cellular compartments such as nuclei, membranes, and cytoplasm. While different segmentation algorithms can be used for each of the sub-cellular compartments, an alternative is to use the same algorithm in different modes. The algorithm in [26] captured a set of bright pixels sharing a common shape distribution. The algorithm used a set of three features, one is the fluorescent emission intensity, and the other two are based on curvature descriptors that are computed from the eigenvalues of the Hessian matrix.

For an image, $I(x, y)$ the eigenvalues $(\lambda_1(x, y) \leq \lambda_2(x, y))$ of the Hessian matrix encode the curvature information of the image, and provide useful cues for detecting ridge-like membrane structures, or blob-like nuclei structures. However, the eigenvalues are dependent on image brightness. The following two curvature-based features are independent of image brightness:

$$\theta(x, y) = \text{atan2}\left(\lambda_1(x, y), \lambda_2(x, y)\right), \tag{4.2}$$

$$\phi(x, y) = \tan^{-1}\frac{\left(\lambda_1(x,y)^2 + \lambda_2(x,y)^2\right)^{1/2}}{I(x, y)}, \tag{4.3}$$

and referred to as shape index, and normalized-curvature index, respectively. This is essentially the same as defining the eigenvalues in a polar coordinate system. This transformation also results in bounded features, $-3\pi/4 \leq \theta(x, y) \leq \pi/4$ and $0 \leq \phi(x, y) \leq \pi/2$.

The estimation process starts with the expected distributions of the shape index for the structures to be segmented. For example, for bright membrane and vessel like structures the shape index is close to $-\pi/2$, because the smaller eigenvalue is negative and the larger eigenvalue approaches to zero. On the other hand, for the blob-like nuclei structures, the shape index is close to $-3\pi/4$, because both eigenvalues are negative and close in value. For both structures, positive values indicate a pixel being more like a background. These constraints are used to compute the initial foreground and background sets for membrane and nuclei structures. An initial segmentation based on the shape index and the normalized-curvature index separates the image pixels into three subsets: background, foreground, and indeterminate. The indeterminate subset comprises all the pixels that are not included in the background or foreground subsets. From these subsets, the background and foreground intensity distributions, as well as the intensity log-likelihood functions are estimated. The algorithm keeps iterating by using two out of the three features at a time to estimate the distribution of the feature that is left out. In the final step, these log-likelihood functions are combined to determine the overall likelihood function. A probability map that represents the probability of a pixel being a foreground is calculated.

Cytoplasm can be detected either by using a specific cytoplasmic marker, or can be detected using computational methods using the fact that the cytoplasmic areas are between nuclear and membrane areas. For most cancer tissue types, it is very important to differentiate the epithelial tissue from the stromal and connective tissue, so that for IFC studies the expression levels of most markers in the epithelial regions can be quantified. Computational methods that use the high connectivity of membrane meshes can be used to differentiate the epithelial regions. For the sample images, any connected component larger than 800 pixels is accepted as a part of the epithelial mask. The nuclei set is then separated into epithelial nuclei and stromal nuclei using the epithelial mask. Figure 7.3.b shows the separated epithelial nuclei (bright blue) from the stromal nuclei (dark blue).

EMLDA is an image segmentation method, which uses the Fisher-Rao criterion as the kernel of the expectation maximization (EM) algorithm [80]. Typically, the EM-algorithm is used to estimate the parameters of some parameterized distributions, such as the popular Gaussian mixture models, and assign labels to data in an iterative way. Instead, the EMLDA algorithm uses the Linear Discriminant Analysis (LDA), a supervised classification technique, as the kernel of EM-algorithm and iteratively group data points projected to a reduced dimensional feature space in such a way that the separability across all classes is maximized. In [63], authors successfully applied this approach in the context of histopathological image analysis to achieve the segmentation of digitized H&E stained whole-slide tissue samples.

V. Feature extraction

Research on useful features for disease classification has often been inspired by visual attributes defined by clinicians as particularly important for disease grading and diagnosis. The vast majority of these features are nuclear features, and many have been established as useful in analysis of both cytopathology and histopathology imagery. Other features that assume discriminatory importance include the margin and boundary appearance of ductal, stromal, tubular and glandular structures. While there is a compilation of features for cytopathology imagery [81], there is relatively little such work for histopathology imagery.

Humans' concept of the world is inherently object-based, as opposed to the largely pixel-based representation of computer vision. As such, human experts describe and understand images in terms of such objects. For pathologists, diagnosis criteria are inevitably described using terms such as "nucleus" and "cell." It is thus important to develop computer vision methods capable of such object-level analysis.

5.1 Object Level Features

Fundamentally, object-level analysis depends greatly on some underlying segmentation mechanism. It is the segmentation methodology that determines what constitutes an object. Commonly, an object is defined as a connected group of pixels satisfying some similarity criterion. The main focus is often on the segmentation of nuclei; there exists little work that explicitly uses features of cytoplasm and stroma, although some researchers have hinted at the need for such features [82,83]. Preliminary work [84] has demonstrated the feasibility of other histologic features for image classification in H&E stained breast cancer. Madabhushi et al. [64] used cytoplasmic and stromal features to automatically segment glands in prostate histopathology. Moreover, it appears that histologic objects may not need to be perfectly segmented to be properly classified when a list of comprehensive features is used in a feature selection framework [84]. Classification performance in distinguishing between different grades of prostate cancer was found to be comparable using manual and automated gland and nuclear segmentation [64]. These results suggest that perfect segmentation is not a prerequisite for good classification.

Object-level features can be categorized as belonging to one of four categories: size and shape, radiometric and densitometric, texture, and chromatin-specific. While the radiometric and densitometric, texture, and chromatin-specific features could be considered low-level features that can be extracted from local neighborhoods, the size and shape metrics are true object-level metrics. A summary of object-level features is listed in Table 5.1; definitions for all listed features can be found in reference [84]. These features were compiled from a comprehensive literature search on cytopathology and histopathology image analysis. In addition, various statistics measures for any of the vector quantities are also commonly calculated. Thus, the mean, median, minimum, maximum, standard deviation, skewness, and kurtosis can be calculated for all vector features. For an RGB image, all relevant features are extracted for each individual color channel; hence the total number of object-level features can easily exceed 1000 for the list of features in Table 5.1. It should be noted that these features are most commonly extracted from high-resolution imagery (see next section), but are relevant for any resolution.

An approach that semantically describes histopathology images using model based intermediate representation (MBIR) and incorporates low-level color texture analysis was presented in [85]. In this approach, basic cytological components in the image are first identified using an unsupervised clustering in the La*b* color space. The connected components of nuclei and cytoplasm regions were modeled using ellipses. An extensive set of features can be constructed from this intermediate representation to characterize the tissue

morphology as well as tissue topology. Using this representation, the relative amount and spatial distribution of these cytological components can be measured. In the application of follicular lymphoma grading, where the spatial distribution of these regions varies considerably between different histological grades, MBIR provides a convenient way to quantify the corresponding observations. Additionally, low-level color texture features are extracted using the co-occurrence statistics of the color information. Due to the staining of the tissue samples, the resulting digitized images have considerably limited dynamic ranges in the color spectrum. Taking this fact into account, a non-linear color quantization using self-organizing maps (SOM) is used to adaptively model the color content of microscopic tissue images. The quantized image is used to construct the co-occurrence matrix from which low-level color texture features are extracted. By combining the statistical features constructed from the MBIR with the low-level color texture features, the classification performance of the system can be improved significantly.

Figure 5.1 shows some of the textural image features for discriminating between benign breast epithelial tissue [78] (DCIS, Figure 5.1a) and DCIS (Figure 5.1d). Figures 5.1b, e show the corresponding Gabor filter responses while Figures 5.1c, f show the corresponding Haralick feature images.

5. 2: Spatially Related Features

Graphs are efficient data structures to represent spatial data and an effective way to represent *structural information* by defining a large set of topological features. Formally, a simple graph $G = (V, E)$ is an undirected and un-weighted graph without self-loops, with V and E being the node and edge set of graph G, respectively.

Application of graph theory to other problem domains is impressive. Real-world graphs of varying types and scales have been extensively investigated in technological [86], social [87] and biological systems [88]. In spite of their different domains, such self-organizing structures unexpectedly exhibit common classes of descriptive spatial (topological) features. These features are quantified by definition of computable metrics.

The use of spatial-relation features for quantifying cellular arrangement was proposed in the early 1990's [89], but didn't find application to clinical imagery until recently. Graphs have now been constructed for modeling different tissue states and to distinguish one state from another by computing metrics on these graphs and classifying their values. Overall, however, the use of spatial arrangement of histological entities (generally at low resolutions) is relatively new, especially in comparison to the wealth of research on nuclear features (at higher resolutions) that has occurred during the same timeframe. A compilation of all the spatial-relation features published in the literature is summarized in Table 5.2. Definitions for all graph structures and features can be found in reference [84]. The total number of spatial-relation features extracted is approximately 150 for all graph structures.

Graph theoretical metrics that can be defined and computed on a cell-graph induce a rich set of descriptive features that can be used for tissue classification. These features provide structural information to describe the tissue organization such as: (i) the distribution of local information around a single cell cluster (e.g., degree, clustering coefficient, etc), (ii) the distribution of global information around a single cell cluster (e.g., eccentricity, closeness, between-ness, etc.), (iii) the global connectivity information of a graph (e.g., ratio of the giant connected component over the graph size, percentage of the isolated and end data points in the graph, etc), (iv) the properties extracted from the spectral graph theory (e.g., spectral radius, eigen exponent, number of connected components, sum of the eigenvalues in the spectrum, etc). Refer to Table 5.2 for a list of commonly extracted graph features.

5.2.1 2D Cell-graph construction—In cell-graph generation as proposed in [90], there are three steps: (i) color quantization, (ii) node identification, and (iii) edge establishment. In the first step, the pixels belonging to cells from those of the others are distinguished. These steps are explained in the next sub-sections.

i. Node identification:

The class information of the pixels is translated to the node information of a cell-graph. At the end of this step, the spatial information of the cells is translated to their locations in the two-dimensional grid. After computing the probabilities, these are compared against a threshold value.

ii. Edge establishment:

This step aims to model pair-wise relationships between cells by assigning an edge between them. Cells that are in physical contact are considered to be in communication, thus edges can be established between them deterministically. For other node pairs, a probability function is used to establish edges between a pair of nodes randomly. Since structural properties of different tissues (e.g., breast, bone and brain) are quite different from each other, edge establishment must be guided by biological hypothesis.

5.2.2. 3D Cell-graphs—The first step in 3D cell-graph construction is to define the distance between a pair of nodes, which is simply the 3D Euclidean distance between a pair of nodes. Based on this distance definition, edges can be established between a pair of nodes. In addition to the simple spatial distance metrics, a multi-dimensional distance measure can be defined using the cell-level *attributes* that can be provided by sophisticated image analysis and segmentation. Cell-level attributes include: x, y, z *physical contact*, *volume* with respect to number of pixels, *peripheral* (i.e., surface area), *shared border* as percentage of shared voxels relative to total, and *polarity*. Then each node of the 3D cell-graph can be represented by a vector of v-dimensions, each dimension corresponding to an attribute. The *Lp* norm can be used to compute the multidimensional distance between them. Once the notion of distance is determined, edge functions of cell-graphs can be applied to construct 3D cell-graphs. The mathematical properties of cell-graphs in 3D can be calculated as the feature set. Although most of the features defined on 2D cell-graphs can be extended to the 3D case, their calculation is not trivial.

5.2.3 Application of Graph based modeling for different histopathology related applications

A. Graph based Modeling of Extra Cellular Matrix: The Extra Cellular Matrix (ECM) is composed of a complex network of proteins and oligosaccharides that play important roles in cellular activities such as division, motility, adhesion, and differentiation. Recently, a new technique was introduced for constructing ECM-aware cell-graphs that incorporates the ECM information surrounding the cells [91]. ECM-aware cell-graphs aim to preserve the interaction between cells and their surrounding ECM while modeling and classifying the tissues. The ECM-aware cell-graphs successfully distinguish between different types of cells that co-exist in the same tissue sample. For example, in bone tissue samples there are usually several cell types, including blood cells, normal cells, and sometimes fracture cells (e.g., chondrocytes and osteoblasts) and cancerous cells. Since these cells are functionally different from each other, the hypothesis is that they would exhibit different spatial organization and structural relationships in the same tissue. This hypothesis has been validated by showing that ECM-aware cell-graphs yield better classification results for different states of bone tissues than the current state of art. In the construction a color value is assigned to each cell (i.e., vertex) based on the RGB values of its surrounding ECM. This

is done by examining the *k* neighboring pixels in each direction, and computing a dominant color for the ECM surrounding each cell using the RGB values of nearly $4k^2$ neighboring pixels.

B. Application to Discriminating Different States of Brain Tissue: Figure 5.3 shows the cell-graphs of brain tissues exhibiting distinctive graph properties that enable discrimination between the different states of brain tissue.

C. Application to Studying Temporal Activity of Adult Human Mesenchymal Stems Cells in a 3D Collagen Matrix: Figure 5.4 shows relationships between adult human mesenchymal stem cells in a 3D collagen protein matrix over time in culture [91]. The graphs are generated from 3D sections of tissue (900×900×80 μm) imaged using confocal microscopy. The nuclei of stem cells in the constructs were stained and imaged at the time points indicated (0 – 24 hours).

D. Application of Graph Theory to Modeling Cancer Grade: In [93], the Voronoi diagram is constructed from a set of seed-like points that denote the centers of each structure of interest (nuclei). From the Voronoi diagram, two more graphs of interest can be constructed: the Delaunay triangulation, which is created by connecting points that share an edge in the Voronoi diagram, and the minimum spanning tree, which is the series of lines that spans the set of points such that the Euclidean sum of the lengths of the lines is smaller than any other spanning tree. From each of these three graphs, a series of features are calculated that captures the size, shape, and arrangement of the structures of the nuclei. The graph based representations of a Gleason grade 4 prostate histopathology image are shown in Figure 5.5.

5.3. Multi-scale feature extraction

Owing to the density of the data and the fact that pathologists tend to employ a multi-resolution approach to analyzing pathology data, feature values are related to the viewing scale or resolution. For instance at low or coarse scales color or texture cues are commonly used and at medium scales architectural arrangement of individual histological structures (glands and nuclei) start to become resolvable. It is only at higher resolutions that morphology of specific histological structures can be discerned.

In [94,95], a multi-resolution approach has been used for the classification of high-resolution whole-slide histopathology images. The proposed multi-resolution approach mimics the evaluation of a pathologist such that image analysis starts from the lowest resolution, which corresponds to the lower magnification levels in a microscope and uses the higher resolution representations for the regions requiring more detailed information for a classification decision. To achieve this, images were decomposed into multi-resolution representations using the Gaussian pyramid approach [96]. This is followed by color space conversion and feature construction followed by feature extraction and feature selection at each resolution level. Once the classifier is confident enough at a particular resolution level, the system assigns a classification label (e.g., stroma-rich, stroma-poor or undifferentiated, poorly differentiating, differentiating) to the image tile. The resulting classification map from all image tiles forms the final classification map. The classification of a whole-slide image is achieved by dividing into smaller image tiles and processing each image tile independently in parallel on a cluster of computer nodes.

As an example, refer to Figure 5.6, showing a hierarchical cascaded scheme for detecting suspicious areas on digitized prostate histopathology slides as presented in [97].

Figure 5.7 shows the results of a hierarchical classifier for detection of prostate cancer from digitized histopathology. Figure 5.7(a) shows the original images with tumor outlined in black. The next 3 columns show the classifier results at increasing analysis scales. Pixels classified as "non-tumor" at a lower magnification (scale) are discarded at the subsequent higher scale, reducing the number of pixels needed for analysis at higher scales. Additionally, the presence of more discriminating information at higher scales allows the classifier to better distinguish between tumor and non-tumor pixels.

At lower resolutions of histological imagery, textural analysis is commonly used to capture tissue architecture, i.e. the overall pattern of glands, stroma and organ organization. For each digitized histological image several hundred corresponding feature scenes can be generated. Texture feature values are assigned to every pixel in the corresponding image. 3D statistical, gradient, and Gabor filters can be extracted in order to analyze the scale, orientation, and anisotropic information of the region of interest. Filter operators are applied in order to extract features within local neighborhoods centered at every spatial location. At medium resolution, architectural arrangement of nuclei within each cancer grade can be described via several graph-based algorithms. At higher resolutions, nuclei and the margin and boundary appearance of ductal and glandular structures have proved to be of discriminatory importance. Many of these features are summarized in Tables 5.1 and 5.2.

5.4. Feature Selection, Dimensionality Reduction, and Manifold Learning

A. Feature Selection—While humans have innate abilities to process and understand imagery, they do not tend to excel at explaining how they reach their decisions. As such, large feature sets are generated in the hopes that some subset of features incorporates the information used by the human expert for analysis. Therefore, many of the generated features could be redundant or irrelevant. Actually, a large set of features may possibly be detrimental to the classification performance, a phenomenon known as "the curse of dimensionality." Feature selection is a means to select the relevant and important features from a large set of features. This is an increasingly important area of research now that automated quantitative image analysis techniques are becoming more mainstream.

Feature selection in histopathological image analysis provides several benefits in addition to improving accuracy. Since images tend to be relatively large, a smaller subset of features needs to be calculated, reducing the computational complexity of classification algorithms. In some applications, it may be preferable to sacrifice the overall performance slightly if this sacrifice greatly reduces the number of selected features. A smaller number of features would also make it easier to explain the underlying model and improve the chances of generalization of the developed system. Additionally, in a multi-resolution framework, a set of features proven useful at a given resolution may not be relevant at another resolution, even within the same image. A feature selection algorithm helps determine which features should be used at a given resolution.

An optimal feature selection method would require an exhaustive search, which is not practical for a large set of features generated from a large dataset. Therefore, several heuristic algorithms have been developed, which use classification accuracy as the optimality criterion. Well-known feature selection methods include the sequential search methods, namely sequential forward selection (SFS) and sequential backward selection (SBS) [98]. SFS works by sequentially adding the feature that most improves the classification performance; similarly, SBS begins with the entire feature set and sequentially removes the feature that most improves the classification performance. Both SFS and SBS suffer from the "nesting effect" whereby features that are selected (SFS) or discarded (SBS) cannot be revisited in a later step and are thus suboptimal [98]. The use of floating search methods, sequential floating forward search (SFFS) and sequential floating backward search

(SFBS), in which previously selected or discarded features can be re-evaluated at later steps avoids the nesting problem [98]. While these methods still cannot guarantee optimality of the selected feature subset, they have been shown to perform very well compared to other feature selection methods [99] and are, furthermore, much more computationally efficient [98]. SFFS is one of the most commonly encountered feature selection methods in pathology image analysis literature.

More recent feature selection research has focused on such methods as genetic algorithms, simulated annealing, boosting [100] and grafting [101]. A taxonomy of feature selection algorithms is presented in [99]. Genetic algorithms and simulated annealing are applications of traditional optimization techniques to feature selection. Boosting, which will be explained in Section 6.c, basically acts as a greedy feature selection process. Grafting (from "gradient feature testing") [101] is based on an elegant formulation of the feature selection problem, whereby the classification of the underlying data and the feature selection process are not separated. Within the grafting framework, a loss function is used that shows preference for classifiers that separate the data with larger margins. Grafting also provides an efficient framework for selection of relevant features. Feature selection based on a measure of discriminatory power was proposed in [102], whereby the authors compute the discriminatory power of each of the wavelet packet sub-bands (features) using a dissimilarity measure between approximated probability density functions for different classes. Derived features are then sorted according to the discriminatory power values associated with the corresponding features.

B. Dimensionality Reduction—While feature selection aims to select features (and reduce the feature dimensionality) that best optimize some criterion related to the class labels of the data (e.g., classification performance), dimensionality reduction techniques aim to reduce dimensionality based on some other criterion. Three well-known and commonly used methods of linear dimensionality reduction are Principal Component Analysis (PCA), Independent Component Analysis (ICA), and Linear Discriminant Analysis (LDA).

Principal Component Analysis (PCA) [103] looks to find a new orthogonal coordinate system whereby the maximum variance of the data is incorporated in the first few dimensions. Projection of the data onto the individual coordinates encompasses varying degrees of variance; the first coordinate encompasses the largest variance in the data, the second coordinate the next largest variance, and so forth.

On the other hand, the LDA is a supervised method; it thus requires class labels for each data sample, mapping the data onto a lower dimensional subspace that best discriminates data. The goal is to find the mapping, where the sum of distances between samples in different classes is maximized; while the sum of distances between samples in same classes is minimized. LDA can also be formulated in terms of eigenanalysis. A comprehensive discussion of PCA and LDA can be found in [104].

Independent Component Analysis [105], looks to find some mixing matrix such that a mixture of the observations (features) are statistically independent. This provides a stronger constraint on the resulting components than PCA, which only requires that the components be uncorrelated. This is why it is particularly well suited for decorrelating independent components from hyperspectral data. Rajpoot & Rajpoot [48] have shown ICA to perform well for extracting three independent components corresponding to three tissue types for segmentation of hyperspectral images of colon histology samples. ICA, however, provides no ranking of the resulting independent components, as does PCA. There are a variety of methods for calculating the independent components (refer to [105]), which are generally

very computationally intensive. ICA is a higher order method that seeks linear projections, not necessarily orthogonal to each other, as in the case of PCA.

C. Manifold Learning—Recently, non-linear dimensionality reduction methods have become popular in learning applications. These methods overcome a major limitation of summarized linear dimensionality reduction methods, which assume that geometrical structure of the high-dimensional feature space is linearized. In reality, high-dimensional feature spaces comprise of highly nonlinear structures and locality preserving dimensionality reduction methods are highly sought after. Manifold learning is a method of reducing a data set from M to N dimensions, where $N < M$ while preserving inter- and intra-class relationships between the data. This is done by projecting the data into a low-dimensional feature space in such a way to preserve high dimensional object adjacency. Many manifold learning algorithms have been constructed over the years to deal with different types of data.

Graph Embedding constructs a confusion matrix Y describing the similarity between any two images C_p and C_p with feature vectors F_p and F_q, respectively, where $p, q \in \{1, 2, ..., k\}$ and k is the total number of images in the data set

$$Y(p, q) = e^{-\|F_p - F_q\|} \in \mathcal{R}^{k \times k} \tag{5.1}$$

The embedding vector X is obtained from the maximization of the function:

$$E_Y(X) = \frac{2\eta X^T (D - Y) X}{X^T D X}, \tag{5.2}$$

where D is the so-called degree matrix, with non-zero values being along the diagonal $D(p, p) = \Sigma_q Y(p, q)$ and $\eta = k - 1$. The k dimensional embedding space is defined by the eigenvectors corresponding to the smallest N eigenvalues of $(D - Y)X = \lambda DX$. The value of N is generally optimized by obtaining classification accuracies for $N \in \{1, 2, \cdots, 10\}$ and selecting the N that provided the highest accuracy for each classification task. For image C, the feature vector F given as input to the Graph Embedding algorithm produces an N-dimensional eigenvector $X(C) = \left[e_j(C) | j \in \{1, 2, ..., N\} \right]$, where $e_j(C)$ is the principal eigenvalue associated with C.

In [93], a Graph Embedding algorithm employing the normalized cuts algorithm was used to reconstruct the underlying manifold on which different breast cancer grades were distributed. Figure 5.8 shows the embedding of different grades of breast cancer histopathology (low, intermediate, high) on the reconstructed manifold; low grades (yellow triangles), intermediate grades (green squares and blue circles), and high grades (red triangles). The manifold captures the biological transformation of the disease in its transition from low to high-grade cancer.

Manifold learning has also been shown to be useful for shape-based classification of prostate nuclei [106]. Rajpoot *et al.* [106] employ Diffusion Maps [107] in order to reduce the dimensionality of shape descriptors down to two dimensions and a fast classification algorithm is derived based on a simple thresholding of the diffusion coordinates.

VI. Classification and subcellular quantification

For histopathology imagery, unlike some other applications of image analysis, one of the primary considerations in the choice of a classifier is its ability to deal with large, highly dense datasets. Also due to multiple image scales at which relevant information may be extracted from histological imagery, use of an ensemble of classifiers as opposed to a single classifier has been proposed.

6.1. Multi-classifier Ensemble Schemes

Theoretical and empirical results alike have established that, in terms of accuracy, ensembles of classifiers generally outperform monolithic solutions. Learning ensembles or Multiple Classifier systems are methods for improving classification accuracy through aggregation of several similar classifiers' predictions and thereby reducing either the bias or variance of the individual classifiers [108].

6.1.A Support Vector Machines (SVM)—SVMs project a set of training data E representing two different classes into a high-dimensional space by means of a kernel function **K**. The algorithm then generates a discriminating hyper-plane to separate out the classes in such a way to maximize a cost function. Testing data is then projected into the high-dimensional space via **K**, and the test data is classified based on where it falls with respect to the hyper-plane. The kernel function $\mathbf{K}(\cdot, \cdot)$ defines the method in which data is projected into the high-dimensional space. A commonly used kernel known as the radial basis function has been employed to distinguish between 3 different prostate tissue classes [109]. Radial basis functions with a grid search for their parameters have also been used to differentiate colon adenocarcinoma histopathology images from benign histopathology images [110] and to classify four different subtypes of meningioma [102].

6.1.B Adaboost—The AdaBoost is an adaptive algorithm in the sense it combines a number of weak classifiers to generate a strong classifier. Image pixels determined as diseased by a pathologist during the training stage are used to generate probability density functions (pdfs) for each of the individual texture features Φ_j, for $j \in \{ 1, ..., K\}$ which are considered as weak classifiers [111]. Bayes Theorem is then used to generate likelihood scenes $L_j = (C_j , l\, j \in \{1, ..., K\})$ for each Φ_j which constitute the weak learners. These are combined by the AdaBoost algorithm into a strong classifier $\Pi^j = \sum_{i=1}^{T} \alpha_i^j l_i^j$ where for every pixel $c^j \in C^j$, $\Pi^j (c^j)$ is the combined likelihood that pixel c^j belongs to cancer class ω_T, α_i^j is the weight determined during training for feature Φ_i, and T is the number of iterations.

In [111] a hierarchical boosted cascade scheme for detecting suspicious areas on digitized prostate histopathology, inspired by the work of Viola and Jones [112] was presented. Efficient and accurate analysis is performed by first only detecting those areas that are found to be suspicious at lower scales. Analysis at subsequent higher magnifications is limited to those regions deemed to be suspicious at lower scales. Pixels classified as "non-tumor" at a lower magnification (scale) are discarded at the subsequent higher scale, reducing the number of pixels needed for analysis at higher scales. The process is repeated using an increasingly larger number of image features and an increasing classification threshold at each iteration. Qualitative results with a hierarchical Boosted classifier at three different image resolutions are shown in Figure 6.1.

6.2. Disease discrimination based on graph based features

Table 6.1 shows the average accuracy and corresponding standard deviation over 20 runs of randomized cross validation based classification of the diseased-healthy-damaged studies by

using five different approaches: (1) the cell graph approach, (2) The cell-distribution approach in which features are extracted from the spatial distribution of cells without considering their pair-wise spatial relations (i.e., without considering the edge information) (3) The textural approach in which features are derived from the gray-level interdependency of pixels in a tissue image, (4) The intensity-based approach in which features are derived from the intensity values of pixels in a tissue image, and (5) The Voronoi diagram-based approach in which features are extracted by making use of the spatial interrelationships of adjacent cells [113, 114].

6.3. Grade based classification of Histopathology imagery

The classification of histopathology imagery is often the ultimate goal in image analysis, particularly in cancer applications. Features derived from segmented nuclei and glands from histopathology are usually a pre-requisite to extracting higher level information regarding the state of the disease. For instance, the grading of prostate cancer by Jafari-Khouzani and Soltanian-Zadeh [115] yielded 97% accuracy for H&E stained imagery based on features derived from nuclear structures in histopathology. Weyn *et al*. [116] reported 87.1%-96.8% accuracy in the correct diagnosis (3 diagnoses) of Feulgen-stained lung cancer specimens, 79.5%-92.3% accuracy in typing (3 types) malignant mesothelioma, and 74.3%-82.9% accuracy in the prognosis (3 classes of survival time) of malignant mesothelioma cases. Analysis of Feulgen-stained breast tissue sections by van de Wouwer *et al*. [117] found 67.1% accuracy in clasifying nuclei as benign or malignant, but 100% classification on a patient level. Tabesh *et al*. [118] found 96.7% accuracy in discriminating between prostate tissue slides with cancer and no cancer, and 81% accuracy in the discrimination between low and high Gleason grades in the same imagery. Immunohistochemically stained colon mucosa allowed for an accuracy of 92% in classification of benign and malignant images by Esgiar *et al*. [119].

The classification of histopathology imagery using spatial architecture information as presented in Weyn *et al*. [116] resulted in 88.7%-96.8% accuracy in the diagnosis of lung cancer, 94.9% accuracy in the typing of malignant mesothelioma, and 80.0%-82.9% accuracy in the prognosis of malignant mesothelioma for Feulgen-stained lung sections. The analysis of H&E stained brain tissue by Demir *et al*. [113] gave 95.5%-97.1% accuracy in the discrimination between benign and cancerous tissue. Keenan *et al*. [120] reported accuracies of 62.3%-76.5% in the grading of H&E stained cervical tissue.

Figure 6.2 (a) shows the low dimensional embedding of the high dimensional attribute space via locally linear embedding of 20 images representing prostate cancer grades 3 (green circles) and 4 (blue squares). Each image is displayed as a point in 3D eigenspace. The clustering clearly shows very good discrimination between these 2 classes which clinically is the most challenging problem in terms of Gleason grading. Figure 6.2 (b) shows bar plots reflecting the classification accuracy obtained via a supervised classifier in distinguishing between pairs of tissue classes – grade 3\4, grade 3 vs. benign epithelium, and grade 4 vs. benign epithelium via a SVM classifier. Note that in every case the classification accuracy is over 90%.

6.4. Sub-cellular Quantification

Quantifying expression levels of proteins with subcellular resolution is critical to many applications ranging from biomarker discovery, pharmaceutical research, and systems biology to treatment planning. In this section, a fully automated method to quantify the expression levels of target proteins in immunofluorescently stained samples in tissue micro arrays (TMAs) is presented. Kolmogorov-Smirnov (KS) statistics, a well-known method in statistics to test if two distributions are different from each other, can be used to compute the

relative expression levels in each of the epithelial and non-epithelial tissue regions. After the sub-cellular compartments are determined using membrane and nuclear markers, the distribution of target proteins in each of these compartments are calculated. The estimated distribution comprises target distribution from the expressed regions as well as nonspecific background binding and tissue autofluorescence that may have left out after the AF removal step. A signed KS distance (sKS) can be defined as the product of the standard KS distance and a sign function (± 1) to indicate which compartment is expressed. For example if sign function is computed between the nuclear and the membrane expression levels, a negative sKS distance will indicate a nuclear expression, and a positive sign will indicate membrane expression. While the magnitude of the sKS distance indicates how strong the expression level difference is between these compartments, its sign indicates in which compartment the protein is expressed.

The standard KS distance is defined as the maximum separation between the cumulative distribution functions (CDF) of two data sets. The CDF of a target protein in any compartment can be calculated by integrating its intensity distribution estimated using a Parzen window approach with Gaussian kernels. Figure 6.3 (c) shows the CDF of the target distributions shown in Figure 6.3 (a) (green color), on each of the segmented sub-cellular regions; nuclei (blue), membrane (red), and cytoplasm (green) shown in Figure 6.3 (b). The CDF's clearly indicates the over-expression of the nuclear region (blue plot) where approximately 10% of the nuclear pixels express intensity values more than 50, as opposed to a very small percentage for other compartments. The sign of the sKS is determined based on sign of the difference between the CDF of the first compartment and the CDF of the second compartment at the protein expression level with highest CDF separation.

The sKS metric on 123 TMA images from 55 patients (some patients are represented as multiple tissue cores) stained with DAPI (nuclei), pan-cadherin (membrane), keratin (tumor/ epithelial mask), and ER markers were tested. DAPI and pan-cadherin are used to segment the sub-cellular compartments, and keratin to segment the epithelial mask. Then the distribution of the ER protein is calculated on each of the epithelial sub-cellular regions. ER is expected to partially or fully express in the nuclear region for ER positive patients. A target distribution is usually observed mixed with nonspecific expression and auto-fluorescence (AF). The sKS based metric was compared to the majority decision of a group of 19 observers scoring estrogen receptor (ER) status, and achieved 96% detection rate with 90% specificity. The presented methods have applications from diagnostics to biomarker discovery and pharmaceutical research.

VII. looking Ahead: Future trends, open problems

Since histopathological image analysis is inherently a cross-disciplinary area, there are unique challenges to the dissemination of research results. One of these is the wide range of publications in which research is published. While there are a few journals that focus on the automated analysis of medical imagery, the majority of histopathological image analysis tends to be published in the leading journals of the researchers' field (pathology, computer vision, etc.). Additionally, there is a need for more evidence regarding the clinical applicability and importance of automated histopathology image analysis methods. We have mentioned areas throughout this paper for which we anticipate ongoing research to have a clear and tangible affect on clinical and pathology workflow.

Comparison of the various methods presented in the literature is difficult, since each research team uses their own dataset and presents their results with different metrics. There is a great need for standard datasets and ground truth for validation of methods. As an example, researchers at the University of South Florida have put together a database of

digital mammograms[1]. While the variety of conditions studied in histopathology image analysis is greater, it is still important that standard datasets be compiled as well as a standard metric of performance. This will allow for direct comparison of the variety of analysis methods being reported in the literature. An additional complication is the variety of analyses performed on the histopathology imagery. Thus, there is a need for a dataset with ground truth pertaining to all the analyses described in this paper.

Going forward, clinical annotation of histopathology data will be a large bottleneck in the evaluation of histopathology related CAD algorithms. Apart from the time constraints on the pathologist to generate this data, the process should be streamlined with active communication between the image analysis scientists and the clinicians with regard to the sort of annotation required, the format and scale at which the annotation is generated, and the ease with which the data can be shared (since histopathology files typically tend to be very large). For instance the sophistication of annotation required to train a CAD system to distinguish cancerous versus non-cancerous regions on pathology images may be very different than the annotation detail required to train a classifier to distinguish grades of cancer. While for the former problem the annotation could be done on a coarser scale (lower resolution), the latter annotation may require explicit segmentation of glands and nuclei, a far more laborious and time consuming process. Due to the large size of pathological images, usually it is not possible to process the whole image on a single-core processor. Therefore, the whole image may be divided into tiles and each tile is processed independently. As a consequence, automatic load balancing in the distribution of the cases to different processors need to be handled carefully [121]. Additionally, the processing can be accelerated even further by the use of graphical processing units (GPUs), cell blades or any other emerging high performance architecture [122].

Histopathological image analysis system evaluation needs to be carried out in a statistical framework. Depending on whether it is a problem of detection (e.g. nuclei detection) or characterization (e.g. grading), some commonly accepted evaluation methodologies need to be followed. Some of these methods, e.g. receiver operating characteristics (ROC) and free response operating characteristics (FROC) have been successfully used for many years in radiology [123]. These techniques could be adopted or adapted accordingly. The level and detailed of quantitative evaluation will vary as a function of the specific problem being addressed. For instance in order to evaluate a nuclear segmentation algorithm on a digitized histological section containing several tens of thousands of nuclei, it is unreasonable to expect that a human reader will be able to manually annotate all nuclei. Evaluation of the scheme may have to be performed on randomly chosen segments of the image. Similarly, if the ultimate objective of the CAD algorithm is, for instance, cancer grading, perfect segmentation of histological structures may not guarantee perfect grade based classification. Evaluation should hence be tailored towards the ultimate objective that the CAD algorithm is being employed for. Additionally, special attention needs to be paid to clearly separate training and testing datasets and explain the evaluation methodology.

Multi-modal Data Fusion/Registration

While digital pathology offers very interesting, highly dense data, one of the exciting challenges will be in the area of multi-modal data fusion. One of the big open questions, especially as it pertains to personalized medicine will be the use of multi-modal data classifiers to be able to make therapy recommendations. This will require solving questions both in terms of data alignment and in terms of knowledge representation for fusion of

---

[1]http://marathon.csee.usf.edu/Mammography/Database.html

heterogeneous sources of data, in order to answer questions that go beyond just diagnosis, such as theragnosis (therapy prediction) and prognosis.

H&E staining is traditionally used for histopathology imaging. Several other modalities exist for imaging of the tissue, each offering its own advantages and limitations. Combining images from different modalities, therefore, may seem to be an attractive proposition, although it does not come without its own challenges, most importantly registration, not to mention the extra cost associated with imaging, storage, and computational time. Registration of image data across the different modalities and fusion of the information contained therein result in a powerful resource of information for diagnosis and prognosis purposes. Fusion methods have been developed for images from different microscopy imaging methods [26] and micro-scale histopathology and large-scale MR images [124-126].

Madabhushi *et al*. [127] have been developing computerized detection methods for prostate cancer from high resolution multi-modal MRI. A pre-requisite to training a supervised classifier to identify prostate cancer (CaP) on MRI is the ability to precisely determine spatial extent of CaP on the radiological imaging modality. CaP can be precisely determined on whole mount histopathology specimens (Fig. 7.1 (a)) which can then be mapped onto MRI (Fig. 7.1 (b)). Figure 7.1 (c) shows the result of registering (Figure 7.1 (b)) the 2D *MRI* slice to the histological section (Figure 7.1 (a)). This requires the use of sophisticated and robust multi-modal deformable registration methods to account for (a) deformations and tissue loss in the whole mount histological specimens during acquisition, and (b) ability to overcome intensity and feature differences between the two modalities (histopathology and MRI). In [124,125] a rigid registration scheme called combined feature ensemble based mutual information (COFEMI) was presented that used alternate feature representations of the target and source images to be registered to facilitate the alignment.

Correlating histological signatures with protein and gene expression

Multiplexing, imaging of a tissue sample with several antibodies simultaneously, allows correlation of characteristic patterns in histopathology images to expression of proteins. Teverovskiy *et al*. [128] recently proposed a novel scheme for automated localization and quantification of the expression of protein biomarkers using a DAPI counter-stain and three other biomarkers. They showed it to be useful for predicting recurrence of prostate cancer in patients undergoing prostatectomy. Recently, it has become clear that information regarding expression of certain proteins related to the onset of cancer is not sufficient. Analyzing multiple-stained histopathology images can help identify oncogenesis-induced changes in sub-cellular location patterns of proteins. Glory *et al*. [129] proposed a novel approach to compare the sub-cellular location of proteins between normal and cancerous tissues. Such a method can also be used for identification of proteins to be used as potential biomarkers.

Exploratory histopathology image analysis

Exploratory analysis of histopathology images can help in finding salient diagnostic features used by humans, associating them with the computed features, and visualizing relationships between different features in high-dimensional spaces. Lessmann *et al*. [130] have proposed the use of self-organizing maps (SOMs) for exploratory analysis of their wavelet-based feature space. The SOM-based visualization of the feature space allowed the authors of [130]to establish a correlation between single features and histologically relevant image structures, making the selection of a subset of clinically important features possible. Iglesias-Rozas and Hopf [131] showed that SOMs can be effectively employed to correctly classify different subtypes of human Glioblastomas (GB) and also to select significant histological and clinical or genetic variables. Alternatively, dimensionality reduction

methods may offer a way of looking at trends and patterns in the data in a reduced dimensional space [132-134].

Computer-aided Prognosis

The use of computer-aided diagnosis for digitized histopathology could begin to be employed for *disease prognostics,* allowing physicians to predict which patients may be susceptible to a particular disease and also predicting disease outcome and survival. For instance, since grade is known to be correlated to outcome (high grade correlates to worse outcome), image based predictors could be used to predict disease recurrence and survival based on analysis of biopsy specimens alone. This would have significant translational implications in that; more expensive molecular assays may not be required for predicting disease.

While there may be a small minority of researchers who are experts in both computer vision and pathology, the vast majority of histopathology image analysis researchers are computer vision researchers. As such, it is important to maintain a constant collaboration with clinical and research pathologists throughout the research process. There are unique challenges to analysis of medical imagery, particularly in the performances required for eventual use of the technique in a clinical setting. It is the pathologist who can best provide the feedback on the performance of the system, as well as suggesting new avenues of research that would provide beneficial information to the pathologist community. Additionally, it is the pathologist that is best equipped to interpret the analysis results in light of underlying biological mechanisms which, in turn, may lead to new research ideas. Similarly, where appropriate it might be pertinent to include the oncologist and radiologist within the algorithmic development and evaluation loop as well.

Acknowledgments

Biographies

Metin N. Gurcan (M'90–SM'05) is an assistant professor at the Biomedical Informatics Department of The Ohio State University. Dr. Gurcan received his BSc. and Ph.D. degrees in Electrical and Electronics Engineering from Bilkent University, Turkey and his MSc. Degree in Digital Systems Engineering from the University of Manchester Institute of Science and Technology, England. He is the recipient of the British Foreign and Commonwealth Organization Award, Children's Neuroblastoma Cancer Foundation Young Investigator Award and National Cancer Institute's caBIG Embodying the Vision Award. During the winters of 1996 and 1997 he was a visiting researcher at the University of Minnesota, Minneapolis. From 1999 to 2001, he was a postdoctoral research fellow and later a research investigator in the Department of Radiology at the University of Michigan, Ann Arbor. Prior to joining the Ohio State University in October 2005, he worked as a senior researcher and product director at a high-tech company, specializing in computer-aided detection and diagnosis of cancer from radiological images.

Dr. Gurcan is a senior member of IEEE, SPIE and RSNA. Dr. Gurcan currently manages several image analysis related projects funded by the National Cancer Institute, National Library of Medicine, American Cancer Society, Department of Defense and Children's Neuroblastoma Cancer Foundation. He teaches tutorials IEEE ICIP and ICASSP conferences, and is the organizer of and lecturer at several meetings, workshops, special focus sessions at leading conferences in areas of image analysis.

Laura E. Boucheron (M'00) received a Bachelor of Science in electrical engineering from New Mexico State University, Las Cruces, NM, USA in 2001 and a Master of Science in electrical engineering from New Mexico State University in 2003. She received a Ph.D. in electrical and computer engineering from the University of Santa Barbara, Santa Barbara, CA, USA in 2008.

She is currently a Postdoctoral Fellow at New Mexico State University in the Klipsch School of Electrical and Computer Engineering. She has previous intern and graduate research assistant experience at both Sandia National Laboratories and Los Alamos National

Laboratory. Her main research interests include high-level image analysis and pattern classification, with special interest in pathology imagery (histo- and cyto-pathology).

Ali Can received the PhD degree in computer and systems engineering, and the MS degree in electrical engineering, both from Rensselaer Polytechnic Institute, Troy, NY, USA, in 1997 and 2000, respectively. He received the BS degree in electrical engineering from the University of Gaziantep, Turkey, in 1993.

He has been a Researcher at visualization and computer vision lab., General Electric (GE) Global Research Center, Niskayuna, NY, since 2004. Before joining GE, Dr. Can was a postdoctoral researcher at Woods Hole Oceanographic Institution, Woods Hole, MA.

Dr. Can has been working on diverse machine vision application areas from industrial inspection to medical imaging, and from life science applications to personalized medicine. His research interests include image enhancement, analysis, registration, and segmentation, quantitation, limited angle tomography, inverse problems, and statistics. Some of the application areas of Dr. Can's work include molecular cell biology for cancer research, molecular pathology, histopathology, quantitation of Parkinson's disease, mammography, non-destructive testing of industrial parts, underwater imaging, 3D confocal microscopy, and retinal fundus imaging. Dr. Can is awarded the Best Paper Award at the 1999 IEEE Conference on Computer Vision and Pattern Recognition. He received the Microscopy Society of America Presidential Student Award, and the Allen B. Dumont Prize for his doctoral work, both in 2000. In Summer 2003, he participated in an underwater archaeology cruise in Black Sea with Dr. Robert Ballard, and a deepwater coral reefs research in US Virgin Islands with Dr. Hanumant Singh.

Anant Madabhushi is the Director of the Laboratory for Computational Imaging and Bioinformatics (LCIB), Department of Biomedical Engineering, Rutgers University. Dr. Madabhushi received his Bachelors Degree in Biomedical Engineering from Mumbai University, India in 1998 and his Masters in Biomedical Engineering from the University of Texas, Austin in 2000. In 2004 he obtained his PhD in Bioengineering from the University of Pennsylvania. He joined the Department of Biomedical Engineering, Rutgers University as an Assistant Professor in 2005. He is also a member of the Cancer Institute of New Jersey and an Adjunct Assistant Professor of Radiology at the Robert Wood Johnson Medical Center, NJ. Dr. Madabhushi has over 60 publications and book chapters in leading International journals and peer-reviewed conferences and patents pending in the areas of medical image analysis, computer-aided diagnosis, machine learning, and computer vision and in applying these techniques for early detection and diagnosis of prostate and breast cancer from high resolution MRI, MR spectroscopy, protein- and gene-expression studies and digitized tissue histopathology. He is also the recipient of a number of awards for both research as well as teaching, including the Busch Biomedical Award (2006), the Technology Commercialization Award (2006), the Coulter Phase 1 and Phase 2 Early Career award (2006, 2008), the Excellence in Teaching Award (2007-2009), the Cancer Institute of New Jersey New Investigator Award (2007), the Society for Imaging Informatics in Medicine (SIIM) New Investigator award (2008), and the Life Sciences Commercialization Award (2008). In addition his research work has also received grant funding from the National Cancer Institute (NIH), New Jersey Commission on Cancer Research, and the Department of Defense.
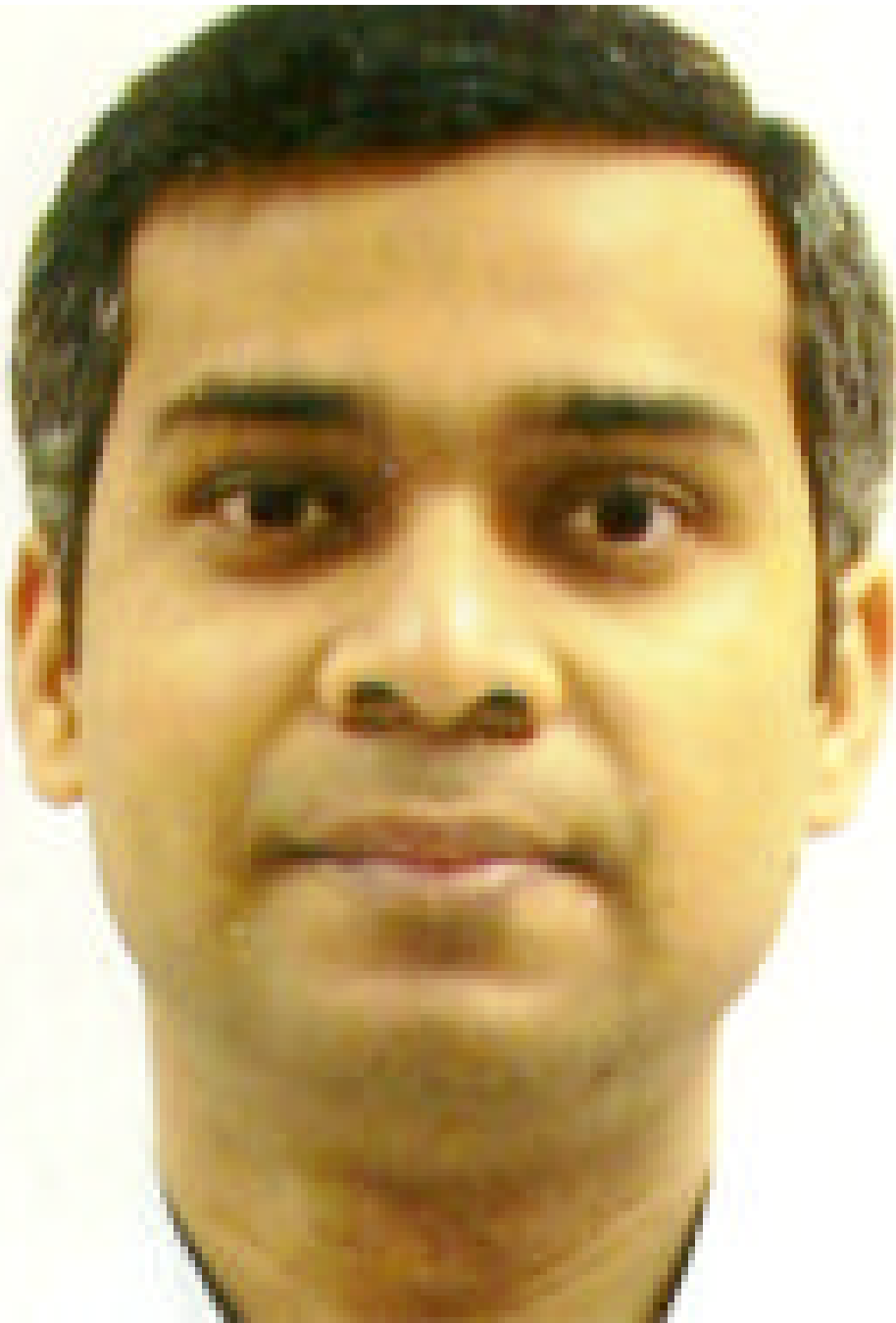
Nasir Rajpoot (M'01) was born in Multan, Pakistan. He graduated with BSc in Mathematics (1991) and MSc in Computer Science (1994) from Bahauddin Zakariya University (Pakistan), and MSc in Systems Engineering from Quaid-e-Azam University (Pakistan) in 1996. He obtained his PhD degree in Computer Science from University of Warwick (UK) in 2001, while being a visiting student at the Applied Mathematics program of Yale University (USA) during 1998-2000.

He joined the University of Warwick as a Lecturer in Computer Science in 2001. Since 2006, he is an Associate Professor in Computer Science at the University of Warwick. He

has published on image coding and denoising. His current research interests are histology image analysis, texture analysis, multiresolution representations, and pattern analysis.

Bülent Yener (SM'02) is a Professor in the Department of Computer Science and Co-Director of Pervasive Computing and Networking Center at Rensselaer Polytechnic Institute in Troy, New York.

He received MS. and Ph.D. degrees in Computer Science, both from Columbia University, in 1987 and 1994, respectively. Before joining RPI, Dr. Yener was a Member of the Technical Staff at the Bell Laboratories in Murray Hill, New Jersey.

Professor Yener's current research interests include bioinformatics, medical informatics, and security and privacy. He has been serving on the Technical Program Committees of leading IEEE conferences and workshops. Currently, he is an associate editor of ACM/Kluwer Winet journal and the IEEE Network Magazine. Dr. Yener is a Member of the IEEE Communications and Computer Society.

References

1. Mendez AJ, Tahoces PG, Lado MJ, Souto M, Vidal JJ. Computer-aided diagnosis: automatic detection of malignant masses in digitized mammograms. Med Phys Jun;1998 25:957–64. [PubMed: 9650186]

2. Tang J, Rangayyan R, Xu J, El Naqa I, Yang Y. Computer-Aided Detection and Diagnosis of Breast Cancer with Mammography: Recent Advances. IEEE Trans Inf Technol Biomed. Jan 20;2009

3. Rubin, R.; Strayer, D.; Rubin, E.; McDonald, J. Rubin's pathology: clinicopathologic foundations of medicine. Lippincott Williams & Wilkins; 2007.

4. Weind KL, Maier CF, Rutt BK, Moussa M. Invasive carcinomas and fibroadenomas of the breast: comparison of microvessel distributions--implications for imaging modalities. Radiology Aug;1998 208:477–83. [PubMed: 9680579]

5. Bartels PH, Thompson D, Bibbo M, Weber JE. Bayesian belief networks in quantitative histopathology. Anal Quant Cytol Histol Dec;1992 14:459–73. [PubMed: 1292445]

6. Hamilton PW, Anderson N, Bartels PH, Thompson D. Expert system support using Bayesian belief networks in the diagnosis of fine needle aspiration biopsy specimens of the breast. J Clin Pathol Apr;1994 47:329–36. [PubMed: 8027370]

7. Allsbrook WC Jr. Mangold KA, Johnson MH, Lane RB, Lane CG, Epstein JI. Interobserver reproducibility of Gleason grading of prostatic carcinoma: general pathologist. Hum Pathol Jan; 2001 32:81–8. [PubMed: 11172299]

8. King CR, Long JP. Prostate biopsy grading errors: a sampling problem? Int J Cancer Dec 20;2000 90:326–30. [PubMed: 11180135]

9. Djavan B, Kadesky K, Klopukh B, Marberger M, Roehrborn CG. Gleason scores from prostate biopsies obtained with 18-gauge biopsy needles poorly predict Gleason scores of radical prostatectomy specimens. Eur Urol 1998;33:261–70. [PubMed: 9555550]

10. Ruijter E, van Leenders G, Miller G, Debruyne F, van de Kaa C. Errors in histological grading by prostatic needle biopsy specimens: frequency and predisposing factors. J Pathol Oct;2000 192:229–33. [PubMed: 11004700]

11. Egevad L, Allsbrook WC Jr. Epstein JI. Current practice of Gleason grading among genitourinary pathologists. Hum Pathol Jan;2005 36:5–9. [PubMed: 15712175]

12. Ladekarl M. Objective malignancy grading: a review emphasizing unbiased stereology applied to breast tumors. APMIS Suppl 1998;79:1–34. [PubMed: 9645191]

13. Daniel, MG.; Luthringer, J. Gleason Grade Migration: Changes in Prostate Cancer Grade in the Contemporary Era. Vol. 9.3. Departments of Pathology and Medicine; Cedars-Sinai, Los Angeles: 2001. Reprinted from PCRI Insights

14. Stamey, F. S. F. Thomas A.; McNeal, John E.; Redwine, Elise A.; Whittemore, Alice S.; Schmid, Hans-Peter. Localized prostate cancer. Relationship of tumor volume to clinical significance for treatment of prostate cancer. Cancer 1993;71:933–938. [PubMed: 7679045]

15. Giger ML, Chan HP, Boone J. Anniversary paper: History and status of CAD and quantitative image analysis: the role of Medical Physics and AAPM. Med Phys Dec;2008 35:5799–820. [PubMed: 19175137]

16. Haygood TM, Whitman GJ, Atkinson EN, Nikolova RG, Sandoval SY, Dempsey PJ. Results of a survey on digital screening mammography: prevalence, efficiency, and use of ancillary diagnostic AIDS. J Am Coll Radiol Apr;2008 5:585–92. [PubMed: 18359447]

17. Schulz-Wendtland R, Hermann KP, Wacker T, Bautz W. [Current situation and future perspectives of digital mammography]. Radiologe Apr;2008 48:324–34. [PubMed: 18335192]

18. Azari A, Nikzad S. Computer-assisted implantology: historical background and potential outcomes-a review. Int J Med Robot Jun;2008 4:95–104. [PubMed: 18348182]

19. Sardanelli F, Giuseppetti GM, Canavese G, Cataliotti L, Corcione S, Cossu E, Federico M, Marotti L, Martincich L, Panizza P, Podo F, Rosselli Del Turco M, Zuiani C, Alfano C, Bazzocchi M, Belli P, Bianchi S, Cilotti A, Calabrese M, Carbonaro L, Cortesi L, Di Maggio C, Del Maschio A, Esseridou A, Fausto A, Gennaro M, Girometti R, Ienzi R, Luini A, Manoukian S, Morassutt S, Morrone D, Nori J, Orlacchio A, Pane F, Panzarola P, Ponzone R, Simonetti G, Torricelli P, Valeri G. Indications for breast magnetic resonance imaging. Consensus document "Attualita in senologia", Florence 2007. Radiol Med Dec;2008 113:1085–1095. [PubMed: 18953635]

20. Doi K. Computer-aided diagnosis in medical imaging: historical review, current status and future potential. Comput Med Imaging Graph Jun-Jul;2007 31:198–211. [PubMed: 17349778]

21. Sakka E, Prentza A, Koutsouris D. Classification algorithms for microcalcifications in mammograms (Review). Oncol Rep 2006;15:1049–55. Spec no. [PubMed: 16525699]

22. Zhu LR, Zhang Y, Wang XY, Liao QP. [Assessment of magnetic resonance imaging in preoperative staging of endometrial carcinoma]. Beijing Da Xue Xue Bao Jun 18;2006 38:249–51. [PubMed: 16778965]

23. Roque AC, Andre TC. Mammography and computerized decision systems: a review. Ann N Y Acad Sci Dec;2002 980:83–94. [PubMed: 12594083]

24. Fox H. Is H&E morphology coming to an end? British Medical Journal 2000;53:38.

25. Camp R, Chung G, Rimm D. Automated subcellular localization and quantification of protein expression in tissue microarrays. Nature Medicine 2002;8:1323–1328.

26. Can, A.; Bello, M.; Tao, X.; Gerdes, M.; Sood, A.; Montalto, M.; Ginty, F. Microscopic Image Analysis for Life Science Applications. Artech House; 2008. Techniques for cellular quantitation of cancer biomarkers.

27. Ginty F, Adak S, Can A, Gerdes M, Larsen M, Cline H, Filkins R, Pang Z, Li Q, Montalto M. The Relative Distribution of Membranous and Cytoplasmic Met Is a Prognostic Indicator in Stage I and II Colon Cancer. Clinical Cancer Research 2008;14:3814. [PubMed: 18559601]

28. Price J, Goodacre A, Hahn K, Hodgson L, Hunter E, Krajewski S, Murphy R, Rabinovich A, Reed J, Heynen S. Advances in molecular labeling, high throughput imaging and machine intelligence portend powerful functional cellular biochemistry tools. Journal of Cellular Biochemistry 2002;87:194–210. [PubMed: 12244572]

29. Can, A.; Bello, M.; Cline, HE.; Tao, X.; Ginty, F.; Sood, A.; Gerdes, M.; Montalto, M. Multi-modal imaging of histological tissue sections. Biomedical Imaging: From Nano to Macro, 2008. ISBI 2008; 5th IEEE International Symposium on; 2008. p. 288-291.

30. Schubert W, Bonnekoh B, Pommer A, Philipsen L, Bockelmann R, Malykh Y, Gollnick H, Friedenberger M, Bode M, Dress A. Analyzing proteome topology and function by automated multidimensional fluorescence microscopy. Nature Biotechnology 2006;24:1270–1278.

31. Newberg J, Murphy R. A Framework for the Automated Analysis of Subcellular Patterns in Human Protein Atlas Images. J. Proteome Res 2008;7:2300–2308. [PubMed: 18435555]

32. Rabinovich A, Agarwal S, Laris C, Price J, Belongie S. Unsupervised Color Decomposition of Histologically Stained Tissue Samples. Advances in Neural Information Processing Systems 16:667–674.

33. Fernandez D, Bhargava R, Hewitt S, Levin I. Infrared spectroscopic imaging for histopathologic recognition. Nature Biotechnology 2005;23:469–474.

34. Blout E, Fields M. On the Infrared Spectra of Nucleic Acids and Certain of Their Components. Science 1948;107:252–252. [PubMed: 17814727]

35. Blout ER, Mellors RC. Infrared Spectra of Tissues. Science 1949;110:137–138. [PubMed: 17816857]

36. Woernley D. Infrared Absorption Curves for Normal and Neoplastic Tissues and Related Biological Substances. Cancer Research 1952;12:516. [PubMed: 14936025]

37. Hollingworth W, Medina L, Lenkinski R, Shibata D, Bernal B, Zurakowski D, Comstock B, Jarvik J. Interrater Reliability in Assessing Quality of Diagnostic Accuracy Studies Using the QUADAS ToolA Preliminary Assessment. Academic Radiology 2006;13:803–810. [PubMed: 16777553]

38. Howe F, Opstad K. ^{1}H MR spectroscopy of brain tumours and masses. NMR Biomed 2003;16:123–131. [PubMed: 12884355]

39. McIntosh LM, Mansfield JR, Crowson AN, Mantsch HH, Jackson M. Analysis and interpretation of infrared microscopic maps: Visualization and classification of skin components by digital staining and multivariate analysis. Biospectroscopy 1999;5:165–269.

40. McIntosh L, Summers R, Jackson M, Mantsch H, Mansfield J, Howlett M, Crowson A, Toole J. Towards Non-Invasive Screening of Skin Lesions by Near-Infrared Spectroscopy. Journal of Investigative Dermatology 2001;116:175–181. [PubMed: 11168814]

41. Frank C, Redd D, Gansler T, McCreery R. Characterization of human breast biopsy specimens with near-IR Raman spectroscopy. Analytical Chemistry 1994;66:319–326. [PubMed: 8135372]

42. Huang Z, McWilliams A, Lui H, McLean D, Lam S, Zeng H. Near-infrared Raman spectroscopy for optical diagnosis of lung cancer. Int. J. Cancer 2003;107:1047–1052. [PubMed: 14601068]

43. Chowdary M, Kumar K, Kurien J, Mathew S, Krishna C. Discrimination of normal, benign, and malignant breast tissues by Raman spectroscopy. Biopolymers 2006;83:556–569. [PubMed: 16897764]

44. Robichaux-Viehoever A, Kanter E, Shappell H, Billheimer D, Jones H III, Mahadevan-Jansen A. Characterization of Raman Spectra Measured in Vivo for the Detection of Cervical Dysplasia. Applied Spectroscopy 2007;61:986–993. [PubMed: 17910796]

45. Wang T, Triadafilopoulos G, Crawford J, Dixon L, Bhandari T, Sahbaie P, Friedland S, Soetikno R, Contag C. Detection of endogenous biomolecules in Barrett's esophagus by Fourier transform infrared spectroscopy. Proceedings of the National Academy of Sciences 2007;104:158–64.

46. Oliveira A, Bitar R, Silveira L Jr, Zangaro R, Martin A. Near-Infrared Raman Spectroscopy for Oral Carcinoma Diagnosis. Photomedicine and Laser Therapy 2006;24:348–353.

47. Levenson R. Spectral imaging perspective on cytomics. Cytometry, Part A 2006;69A:592–600.

48. Rajpoot, K.; Rajpoot, N. Proceedings. 2004. Hyperspectral Colon Tissue Cell Classification.

49. Woolfe, F.; Maggioni, M.; Davis, G.; Warner, F.; Coifman, R.; Zucker, S. Hyper-spectral microscopic discrimination between normal and cancerous colon biopsies. 2007.

50. Boucheron L, Bi Z, Harvey N, Manjunath B, Rimm D. Utility of multispectral imaging for nuclear classification of routine clinical histopathology imagery. BMC Cell Biology 2007;8:S8. [PubMed: 17634098]

51. Masood K, Rajpoot N. Classification of Hyperspectral Colon Biopsy Images: Does 2D Spatial Analysis Suffice? Annals of the BMVA. 2008

52. Stadlbauer A, Gruber S, Nimsky C, Fahlbusch R, Hammen T, Buslei R, Tomandl B, Moser E, Ganslandt O. Preoperative Grading of Gliomas by Using Metabolite Quantification with High-Spatial-Resolution Proton MR Spectroscopic Imaging. Radiology Mar 1;2006 238:958–969. [PubMed: 16424238]

53. Tiwari, P.; Madabhushi, A.; Rosen, M. Proceedings. 2007. A Hierarchical Unsupervised Spectral Clustering Scheme for Detection of Prostate Cancer from Magnetic Resonance Spectroscopy (MRS); p. 278

54. Yang L, Meer P, Foran D. Unsupervised segmentation based on robust estimation and color active contour models. IEEE Transactions on Information Technology in Biomedicine 2005;9:475–486. [PubMed: 16167702]

55. Narasimha-Iyer H, Can A, Roysam B, Stewart V, Tanenbaum H, Majerovics A, Singh H. Robust detection and classification of longitudinal changes in color retinal fundus images for monitoring diabetic retinopathy. Biomedical Engineering, IEEE Transactions on 2006;53:1084–1098.

56. Bello, M.; Can, A.; Tao, X. Accurate registration and failure detection in tissue micro array images. Biomedical Imaging: From Nano to Macro, 2008. ISBI 2008; 5th IEEE International Symposium on; 2008. p. 368-371.

57. Gleason DF. Histologic grading of prostate cancer: a perspective. Hum Pathol Mar;1992 23:273–9. [PubMed: 1555838]

58. Alexe G, Dalgin GS, Scanfeld D, Tamayo P, Mesirov JP, DeLisi C, Harris L, Barnard N, Martel M, Levine AJ, Ganesan S, Bhanot G. High expression of lymphocyte-associated genes in node-negative HER2+ breast cancers correlates with lower recurrence rates. Cancer Res Nov 15;2007 67:10669–76. [PubMed: 18006808]

59. Bibbo M, Kim DH, Pfeifer T, Dytch HE, Galera-Davidson H, Bartels PH. Histometric features for the grading of prostatic carcinoma. Anal Quant Cytol Histol Feb;1991 13:61–8. [PubMed: 2025375]

60. Belien JA, Baak JP, van Diest PJ, van Ginkel AH. Counting mitoses by image processing in Feulgen stained breast cancer sections: the influence of resolution. Cytometry Jun 1;1997 28:135–40. [PubMed: 9181303]

61. Markiewicz T, Osowski S, Patera J, Kozlowski W. Image processing for accurate cell recognition and count on histologic slides. Anal Quant Cytol Histol Oct;2006 28:281–91. [PubMed: 17067010]

62. Kim YJ, Romeike BF, Uszkoreit J, Feiden W. Automated nuclear segmentation in the determination of the Ki-67 labeling index in meningiomas. Clin Neuropathol Mar-Apr;2006 25:67–73. [PubMed: 16550739]

63. Sont JK, De Boer WI, van Schadewijk WA, Grunberg K, van Krieken JH, Hiemstra PS, Sterk PJ. Fully automated assessment of inflammatory cell counts and cytokine expression in bronchial tissue. Am J Respir Crit Care Med Jun 1;2003 167:1496–503. [PubMed: 12770855]

64. Naik, S.; Doyle, S.; Madabhushi, A.; Tomaszeweski, J.; Feldman, M. Workshop on Microscopic Image Analysis with Applications in Biology Piscataway. NJ: 2007. Automated Gland Segmentation and Gleason Grading of Prostate Histology by Integrating Low-, High-level and Domain Specific Information.

65. Karvelis PS, Fotiadis DI, Georgiou I, Syrrou M. A watershed based segmentation method for multispectral chromosome images classification. Conf Proc IEEE Eng Med Biol Soc 2006;1:3009–12. [PubMed: 17946153]

66. Petushi S, Garcia FU, Haber MM, Katsinis C, Tozeren A. Large-scale computations on histology images reveal grade-differentiating parameters for breast cancer. BMC Med Imaging 2006;6:14. [PubMed: 17069651]

67. Fernandez DC, Bhargava R, Hewitt SM, Levin IW. Infrared spectroscopic imaging for histopathologic recognition. Nat Biotechnol Apr;2005 23:469–74. [PubMed: 15793574]

68. Boucheron LE, Bi Z, Harvey NR, Manjunath B, Rimm DL. Utility of multispectral imaging for nuclear classification of routine clinical histopathology imagery. BMC Cell Biol 2007;8(Suppl 1):S8. [PubMed: 17634098]

69. Singh SS, Qaqish B, Johnson JL, Ford OH 3rd, Foley JF, Maygarden SJ, Mohler JL. Sampling strategy for prostate tissue microarrays for Ki-67 and androgen receptor biomarkers. Anal Quant Cytol Histol Aug;2004 26:194–200. [PubMed: 15457671]

70. Weaver DL, Krag DN, Manna EA, Ashikaga T, Harlow SP, Bauer KD. Comparison of pathologist-detected and automated computer-assisted image analysis detected sentinel lymph node micrometastases in breast cancer. Mod Pathol Nov;2003 16:1159–63. [PubMed: 14614056]

71. Glotsos D, Spyridonos P, Petalas P, Cavouras D, Ravazoula P, Dadioti PA, Lekka I, Nikiforidis G. Computer-based malignancy grading of astrocytomas employing a support vector machine classifier, the WHO grading system and the regular hematoxylin-eosin diagnostic staining procedure. Anal Quant Cytol Histol Apr;2004 26:77–83. [PubMed: 15131894]

72. Wahlby C, Sintorn IM, Erlandsson F, Borgefors G, Bengtsson E. Combining intensity, edge and shape information for 2D and 3D segmentation of cell nuclei in tissue sections. J Microsc Jul;2004 215:67–76. [PubMed: 15230877]

73. Korde VR, Bonnema GT, Xu W, Krishnamurthy C, Ranger-Moore J, Saboda K, Slayton LD, Salasche SJ, Warneke JA, Alberts DS, Barton JK. Using optical coherence tomography to evaluate skin sun damage and precancer. Lasers Surg Med Oct;2007 39:687–95. [PubMed: 17960754]

74. Gurcan, M.; Pan, T.; Shimada, H.; Saltz, JH. APIII 2006 Vancouver, BC. 2006. Image analysis for neuroblastoma classification: Hysteresis thresholding for cell segmentation.

75. Gurcan MN, Pan T, Shimada H, Saltz J. Image analysis for neuroblastoma classification: segmentation of cell nuclei. Conf Proc IEEE Eng Med Biol Soc 2006;1:4844–7. [PubMed: 17947119]

76. Bamford, P.; Lovell, B. Method for accurate unsupervised cell nucleus segmentation. Engineering in Medicine and Biology Society, 2001; Proceedings of the 23rd Annual International Conference of the IEEE; 2001. p. 2704-2708.

77. Begelman, G.; Pechuk, M.; Rivlin, E.; Sabo, E. System for Computer-Aided Multiresolution Microscopic Pathology Diagnostics. Computer Vision Systems, 2006 ICVS '06; IEEE International Conference on; 2006. p. 16-16.

78. Naik, S.; Doyle, S.; Agner, S.; Madabhushi, A.; Tomaszeweski, J.; Feldman, M. ISBI Special Workshop on Computational Histopathology (CHIP). IEEE; Paris, France: 2008. Automated gland and nuclei segmentation for grading of prostate and breast cancer histopatholog; p. 284-287.

79. Sethian, JA. Level Set Methods: Evolving Interfaces in Geometry, Fluid Mechanics, Computer Vision and Materials Sciences. First ed.. Cambridge University Press; 1996.

80. Kong, J.; Shimada, H.; Boyer, K.; Saltz, JH.; Gurcan, M. Image analysis for automated assessment of grade of neuroblastic differentiation. IEEE International Symposium on Biomedical Imaging (ISBI) 2007; Metro Washington, D.C.. April 12-15, 2007; 2007.

81. Rodenacker K, Bengtsson E. A feature set for cytometry on digitized microscopic images. Analytical Cellular Pathology 2003;25:1–36. [PubMed: 12590175]

82. Sims AJ, Bennett MK, Murray A. Image analysis can be used to detect spatial changes in the histopathology of pancreatic tumours. Physics in Medicine and Biology 2003;48:N183–N191. [PubMed: 12884936]

83. Gil J, Wu H, Wang BY. Image Analysis and Morphometry in the Diagnosis of Breast Cancer. Microscopy Research and Technique 2002;59:109–118. [PubMed: 12373721]

84. Boucheron, LE. PhD Thesis. 2008. Object- and Spatial-Level Quantitative Analysis of Multispectral Histopathology Images for Detection and Characterization of Cancer.

85. Sertel O, Kong J, Catalyurek U, Lozanski G, Saltz J, Gurcan M. Histopathological Image Analysis using Model-based Intermediate Representations and Color Texture: Follicular Lymphoma Grading. Journal of Signal Processing Systems. 2009 (in print).

86. Faloutsos, M.; Faloutsos, P.; Faloutsos, C. On power-law relationships of the internet topology. 1999. p. 251-262.

87. Watts D, Strogatz S. Collective dynamics ofsmall-world'networks. Nature 1998;393:440–442. [PubMed: 9623998]

88. Wuchty S, Ravasz E, Barabasi A. The architecture of biological networks. Complex Systems in Biomedicine. 2003

89. Albert R, Schindewolf T, Baumann I, Harms H. Three-Dimensional Image Processing for Morphometric Analysis of Epithelium Sections. Cytometry 1992;13:759–765. [PubMed: 1451606]

90. Bilgin, C.; Demir, C.; Nagi, C.; Yener, B. Cell-Graph Mining for Breast Tissue Modeling and Classification. 2007. p. 5311-5314.

91. Bilgin C, Bullough P, Plopper G, Yener B. ECM Aware Cell-Graph Mining for Bone Tissue Modeling and Analysis. RPI Computer Science Technical Report 08-07. 2008

92. Gunduz C, Yener B, Gultekin S. The cell graphs of cancer. Bioinformatics 2004;20

93. Doyle, S.; Hwang, M.; Shah, K.; Madabhushi, A.; Feldman, M.; Tomaszeweski, J. ISBI. 2007. Automated grading of prostate cancer using architectural and textural image features; p. 1284-1287.

94. Kong J, Sertel O, Shimada H, Boyer K, Saltz J, Gurcan M. Computer-aided evaluation of neuroblatoma on whole-slide histology images: Classifying grade of neuroblastic differentiation. Pattern Recognition 2009;42:1080–1092.

95. Sertel O, Kong J, Shimada H, Catalyurek U, Saltz J, Gurcan MN. Computer-aided prognosis of neuroblastoma on whole-slide images: Classification of stromal development. Pattern Recognition 2009;42:1093–1103. [PubMed: 20161324]

96. Burt P, Adelson E. The Laplacian pyramid as a compact image code. IEEE Transactions on Communications 1983;31:532–540.

97. Doyle S, Madabhushi A, Feldman M, Tomaszewski J. A boosting cascade for automated detection of prostate cancer from digitized histology. Lecture Notes in Computer Science 2006;4191:504.

98. Pudil P, Novovi\vcov\'a J, Kittler J. Floating search methods in feature selection. Pattern Recognition Letters 1994;15:1119–1125.

99. Jain A, Zongker D. Feature Selection: Evaluation, Application, and Small Sample Performance. IEEE Transactions on Pattern Analysis and Machine Intelligence 1997;19:153–158.

100. Freund Y, Shapire RE. A decision-theoretic generalization of on-line learning and an application to boosting. Journal of Computer and System Sciences 1997;55:119–139.

101. Perkins S, Lacker K, Theiler J. Grafting: Fast, Incremental Feature Selection by Gradient Descent in Function Space. Journal of Machine Learning Research 2003;3:1333–1356.

102. Qureshi, H.; Sertel, O.; Rajpoot, N.; Wilson, R.; Gurcan, M. Medical Image Computing and Computer-Assisted Intervention – MICCAI 2008. 2008. Adaptive Discriminant Wavelet Packet Transform and Local Binary Patterns for Meningioma Subtype Classification; p. 196-204.

103. Jolliffe, I. Principal component analysis. 2002.

104. Martinez A, Kak A. Pca versus lda. IEEE Transactions on Pattern Analysis and Machine Intelligence 2001;23:228–233.

105. Hyvärinen A, Oja E. Independent component analysis: algorithms and applications. Neural networks 2000;13:411–430. [PubMed: 10946390]

106. Rajpoot, N.; Arif, M.; Bhalerao, A. Proceedings. 2007. Unsupervised Learning of Shape Manifolds.

107. Coifman R, Lafon S, Lee A, Maggioni M, Nadler B, Warner F, Zucker S. Geometric diffusions as a tool for harmonic analysis and structure definition of data: Diffusion maps. Proceedings of the National Academy of Sciences 2005;102:7426–7431.

108. Kuncheva LI, Whitaker CJ. Measures of Diversity in Classifier Ensembles and Their Relationship with the Ensemble Accuracy. Machine Learning 2003;51:181–207.

109. Doyle, S.; Hwang, M.; Shah, K.; Madabhushi, A.; Tomaszeweski, J.; Feldman, M. Automated Grading of Prostate Cancer using Architectural and Textural Image Features. International Symposium on Biomedical Imaging; Washington DC. 2007. p. 1284-87.

110. Rajpoot, K.; Rajpoot, N. Medical Image Computing and Computer-Assisted Intervention – MICCAI 2004. 2004. SVM Optimization for Hyperspectral Colon Tissue Cell Classification; p. 829-837.

111. Doyle, S.; Rodriguez, C.; Madabhushi, A.; Tomaszeweski, J.; Feldman, M. Detecting Prostatic Adenocarcinoma from Digitized Histology Using a Multi-Scale, Hierarchical Classification Approach. IEEE Engineering in Medicine and Biology Conference; New York City, NY. 2006. p. 4759-62.

112. Viola P, Jones MJ. Robust real-time face detection. International Journal of Computer Vision May;2004 57:137–154.

113. Demir C, Yener B. Automated Cancer Diagnosis Based on histopathological images: a systematic survey. Rensselaer Polytechnic Institute, Troy :NY2006.

114. Gunduz C, Yener B, Gultekin SH. The cell graphs of cancer. Bioinformatics Aug 4;2004 20(Suppl 1):i145–51. [PubMed: 15262793]

115. Jafari-Khouzani K, Soltanian-Zadeh H. Multiwavelet grading of pathological images of prostate. IEEE Trans Biomed Eng Jun;2003 50:697–704. [PubMed: 12814236]

116. Weyn B, Wouver G, Daele A, et al. Automated Breast Tumor Diagnosis and Grading Based on Wavelet Chromatin Texture Description. Cytometry 1998;33:32–40. [PubMed: 9725556]

117. Van de Wouwer G, Weyn B, Scheunders P, Jacob W, Van Marck E, VAN D. Wavelets as chromatin texture descriptors for the automated identification of neoplastic nuclei. Journal of Microscopy 2000;197:25. [PubMed: 10620145]

118. Tabesh A, Teverovskiy M, Pang HY, Kumar VP, Verbel D, Kotsianti A, Saidi O. Multifeature prostate cancer diagnosis and Gleason grading of histological images. IEEE Trans Med Imaging Oct;2007 26:1366–78. [PubMed: 17948727]

119. Esgiar AN, Naguib RN, Sharif BS, Bennett MK, Murray A. Microscopic image analysis for quantitative measurement and feature identification of normal and cancerous colonic mucosa. IEEE Trans Inf Technol Biomed Sep;1998 2:197–203. [PubMed: 10719530]

120. Keenan S, Diamond J, Glenn McCluggage W, Bharucha H, Thompson D, Bartels P, Hamilton P. An automated machine vision system for the histological grading of cervical intraepithelial neoplasia (CIN). J Pathol 2000;192

121. Cambazoglu, B.; Sertel, O.; Kong, J.; Saltz, JH.; Gurcan, MN.; Catalyurek, UV. Efficient processing of pathological images using the grid: Computer-aided prognosis of neuroblastoma. Proceedings of Fifth International Workshop on Challenges of Large Applications in Distributed Environments; Monterey Bay, CA. 2007. p. 35-41.

122. Ruiz A, Sertel O, Ujaldon M, Catalyurek UV, Saltz J, Gurcan MN. Pathological Image Analysis Using the GPU: Stroma Classification for Neuroblastoma. IEEE BIBM'07. 2007

123. Gurcan MN, Chan HP, Sahiner B, Hadjiiski L, Petrick N, Helvie MA. Optimal neural network architecture selection: improvement in computerized detection of microcalcifications. Acad Radiol Apr;2002 9:420–9. [PubMed: 11942656]

124. Chappelow, J.; Viswanath, S.; Madabhushi, A.; Rosen, M.; Tomaszeweski, J.; Feldman, M. SPIE Medical Imaging. San Diego, CA: 2008. Improving Supervised Classification Accuracy using Non-rigid Multimodal Image Registration: Computer-Aided Detection of Prostate Cancer on ex vivo MRI.

125. Chappelow, J.; Madabhushi, A.; Rosen, M.; Tomaszeweski, J.; Feldman, M. SPIE Medical Imaging. Vol. 6512. San Diego: 2007. Multimodal Image Registration of ex vivo 4 Tesla Prostate MRI with Whole Mount Histology for Cancer Detection; p. S1-S12.

126. Ourselin S, Roche A, Subsol G, Pennec X, Ayache N. Reconstructing a 3D structure from serial histological sections. Image and Vision Computing 2001;19:25–31.

127. Madabhushi A, Feldman M, Metaxas D, Tomaszeweski J, Chute D. Automated Detection of Prostatic Adenocarcinoma from High Resolution Ex Vivo MRI. IEEE Trans Med Imaging 2005;24:1611–25. [PubMed: 16350920]

128. Teverovskiy, M.; Vengrenyuk, Y.; Tabesh, A.; Sapir, M.; Fogarasi, S.; Ho-Yuen, P.; Khan, FM.; Hamann, S.; Capodieci, P.; Clayton, M.; Kim, R.; Fernandez, G.; Mesa-Tejada, R.; Donovan, MJ. Automated localization and quantification of protein multiplexes via multispectral fluorescence imaging. Biomedical Imaging: From Nano to Macro, 2008. ISBI 2008; 5th IEEE International Symposium on; 2008. p. 300-303.

129. Glory E, Murphy RF. Automated Subcellular Location Determination and High-Throughput Microscopy. Developmental Cell 2007;12:7–16. [PubMed: 17199037]

130. Lessmann, B.; Degenhard, A.; Kessar, P.; Pointon, L.; Khazen, M.; Leach, M.; Nattkemper, T. Artificial Neural Networks: Biological Inspirations – ICANN 2005. 2005. SOM-Based Wavelet Filtering for the Exploration of Medical Images; p. 671-676.

131. Iglesias-Rozas JR, Hopf N. Histological heterogeneity of human glioblastomas investigated with an unsupervised neural network (SOM). Histol Histopathol Apr;2005 20:351–6. [PubMed: 15736037]

132. Doyle, S.; Hwang, M.; Naik, S.; Feldman, M.; Tomaszeweski, J.; Madabhushi, A. MICCAI. 2007. Using manifold learning for content-based image retrieval of prostate histopathology.

133. Basavanhally, A.; Agner, S.; Alexe, G.; Bhanot, G.; Ganesan, S.; Madabhushi, A. MMBIA Workshop. 2008. Manifold learning with graph-based features for identifying extent of lymphocytic infiltration from high grade breast cancer histology.

134. Lexe G, Monaco J, Doyle S, Basavanhally A, Reddy A, Seiler M, Ganesan S, Bhanot G, Madabhushi A. Towards Improved Cancer Diagnosis and Prognosis Using Analysis of Gene Expression Data and Computer Aided Imaging. Experimental Biology and Medicine August 1;2009 234:860–879. 2009. [PubMed: 19491367]
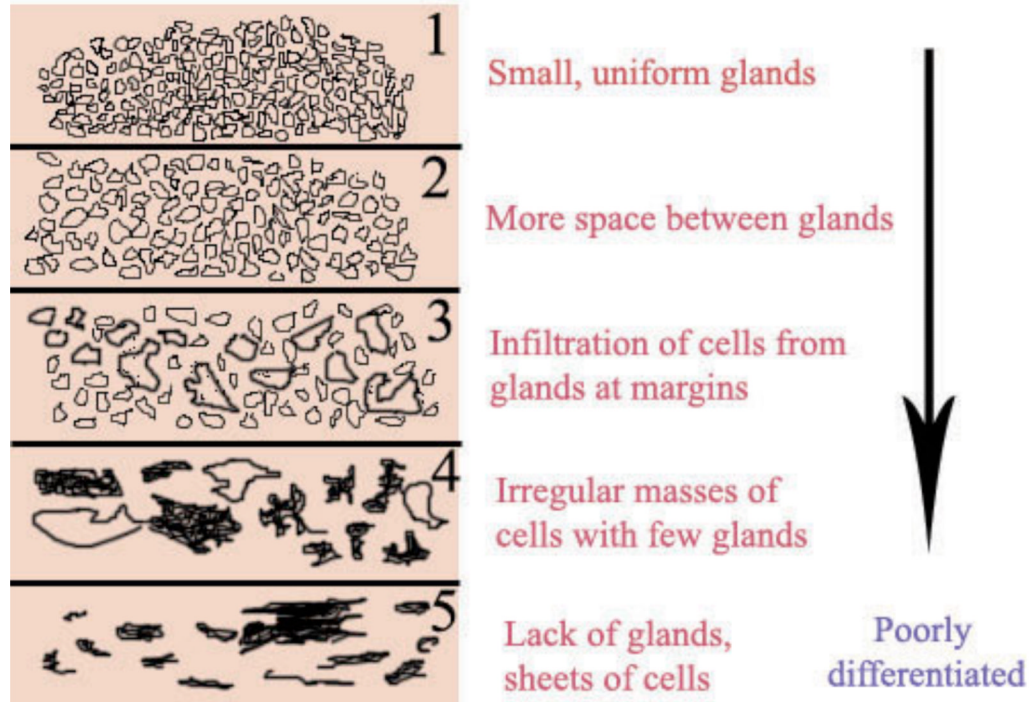
Gleason Scale

Well differentiated

1 Small, uniform glands

2 More space between glands

3 Infiltration of cells from glands at margins

4 Irregular masses of cells with few glands

5 Lack of glands, sheets of cells

Poorly differentiated

Figure 1.1.
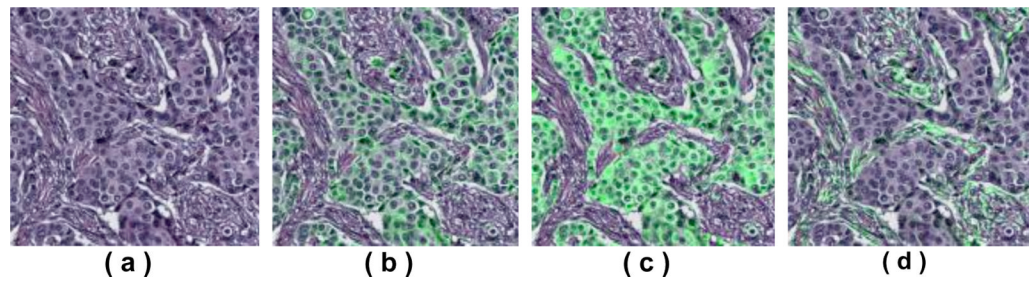Schema showing different cancer grades prevalent in prostate cancer.

Figure 2.1.
(a) H&E image of a breast tumor tissue. Fluorescently labeled markers superimposed as green color on the H&E image, **(b)** β-catenin, **(c)** pan-keratin, and **(d)** smooth muscle α-actin, markers.
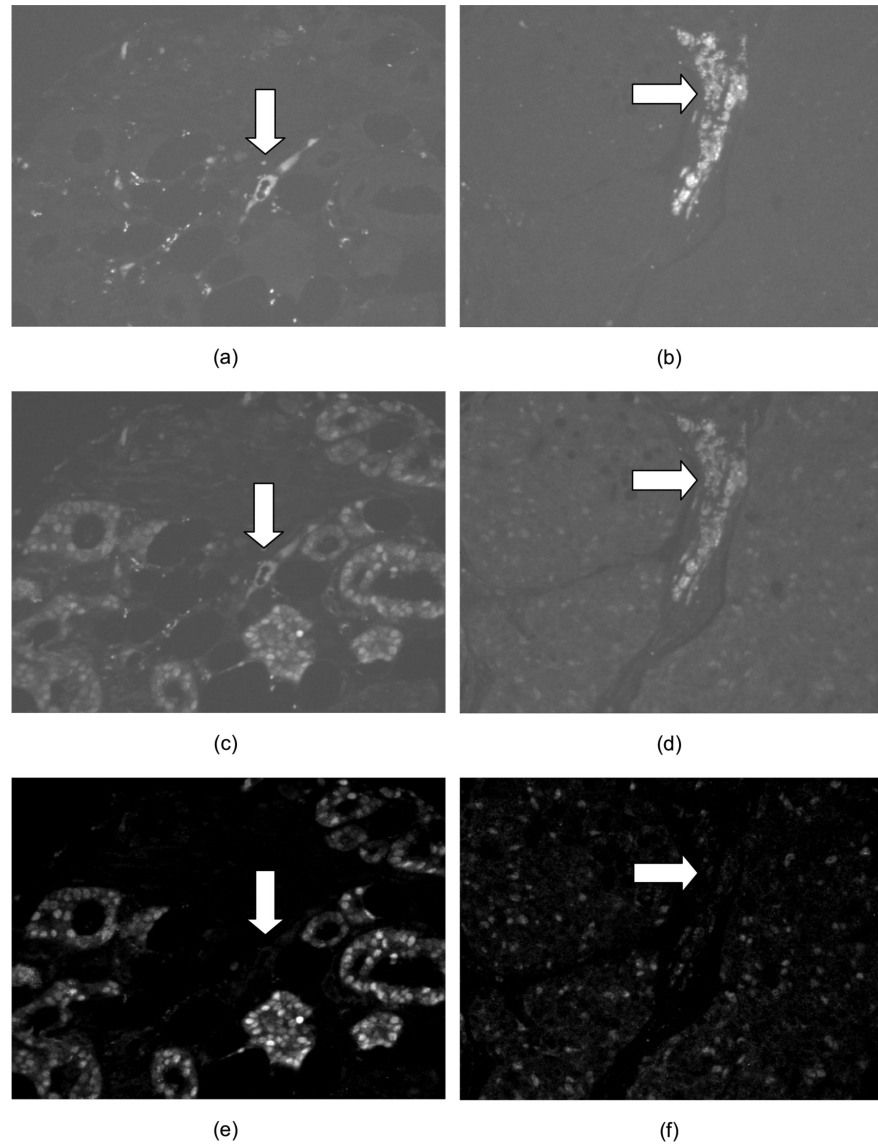
Figure 3.1.
(a,b) Images from the first step acquisition. **(c,d)** Images from the second acquisition. **(e,f)** AF-free corrected images. Cy5 dye **(a, c, e)** is directly conjugated to Pan-Cadherin, a membrane protein. Cy3 dye **(b,d,f)** is directly conjugated to Estrogen Receptor. The arrows point to successfully removed the high-AF regions, such as blood cells and fat

(a) (b) (c) (d)
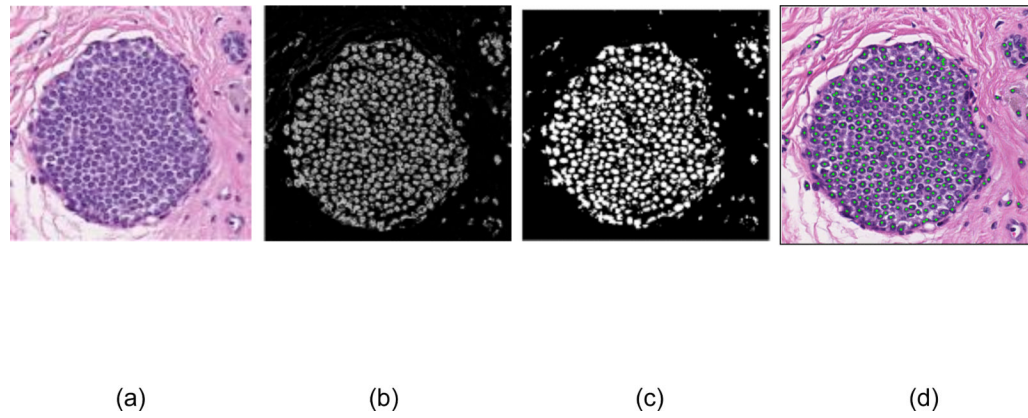
Figure 4.1.
(a) Original DCIS image with corresponding (b) likelihood scene obtained via a Bayesian classifier driven by color and texture, (c) Thresholded version of likelihood scene (95% confidence), (d) The final nuclear segmentation obtained by integrating the Bayesian classifier with the template matching scheme.
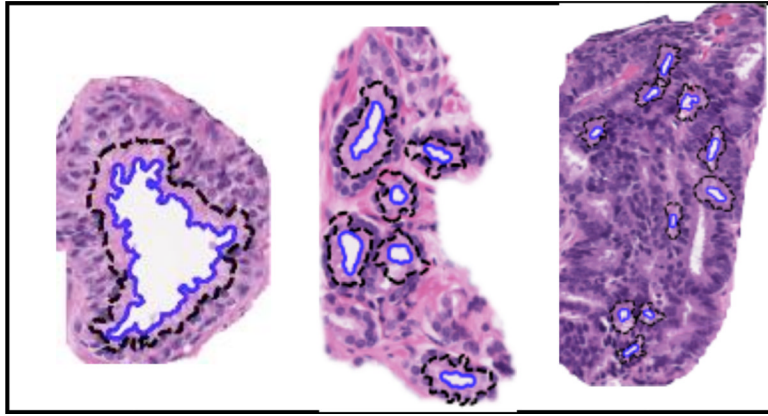
Figure 4.2.
Results of the automatic segmentation algorithm (blue contours – lumen boundary, black contours -- inner boundary of the nuclei of the epithelial cells surrounding the gland). Shown from left to right are example images of benign epithelium, intermediate-, and high grade cancer.
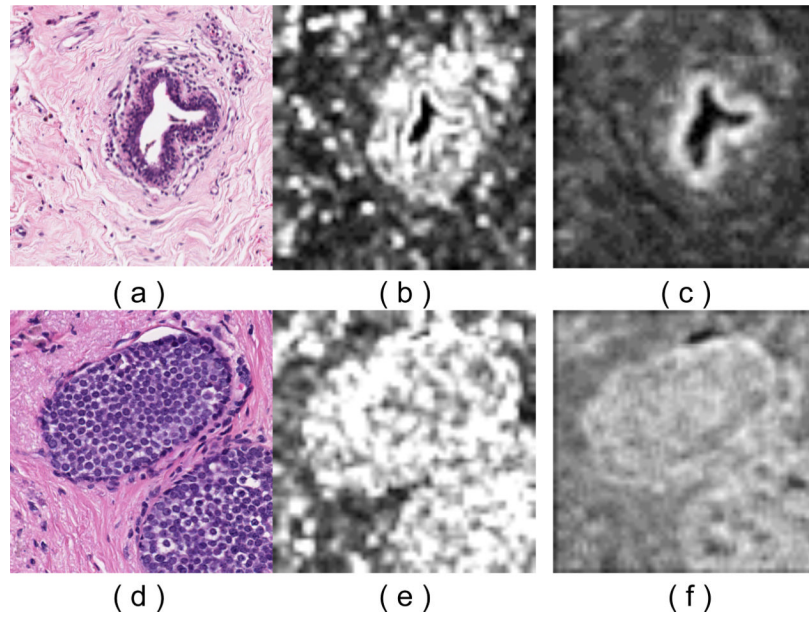
Figure 5.1.
Supervised extraction of histological features to describe tissue appearance of (a) benign epithelium, and (b) DCIS. Feature images for the 2 tissue classes (benign epithelium, DCIS) corresponding to Gabor wavelet features (b, e) and Haralick second order features (c, f) are shown.
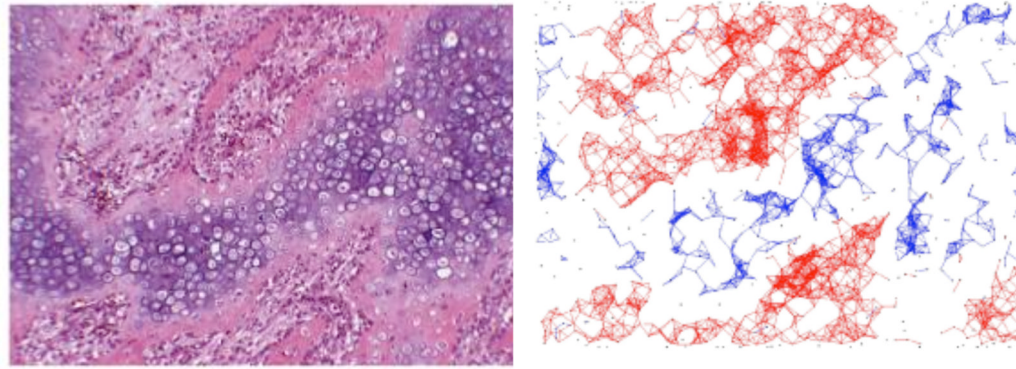
Figure 5.2.
Bone fracture and its corresponding ECM-aware cell-graph representation. Note the presence of a link between a pair of nodes in an ECM–aware cell-graph indicates not only topological closeness but also it implies the similarity in the surrounding ECM [91].
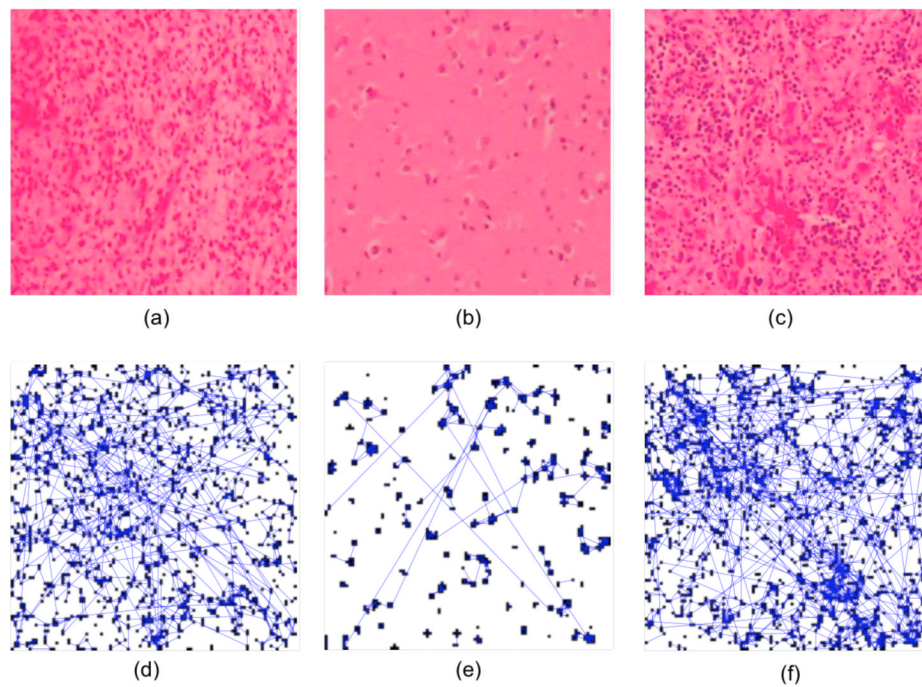
Figure 5.3.
Illustrating the differences between cell-graphs for cancerous, healthy, and inflamed brain tissues. Panels (a)-(c) show brain tissue samples that are (a) cancerous (gliomas), (b) healthy, and (c) inflamed, but non-cancerous. Panels (d)-(f) show the cell-graphs corresponding to each tissue image. While the number of cancerous and inflamed tissue samples appear to have similar numbers and distributions of cells, the structure of their resulting cell-graphs shown in (d) and (f) are dramatically different. (Figure is taken from [92])
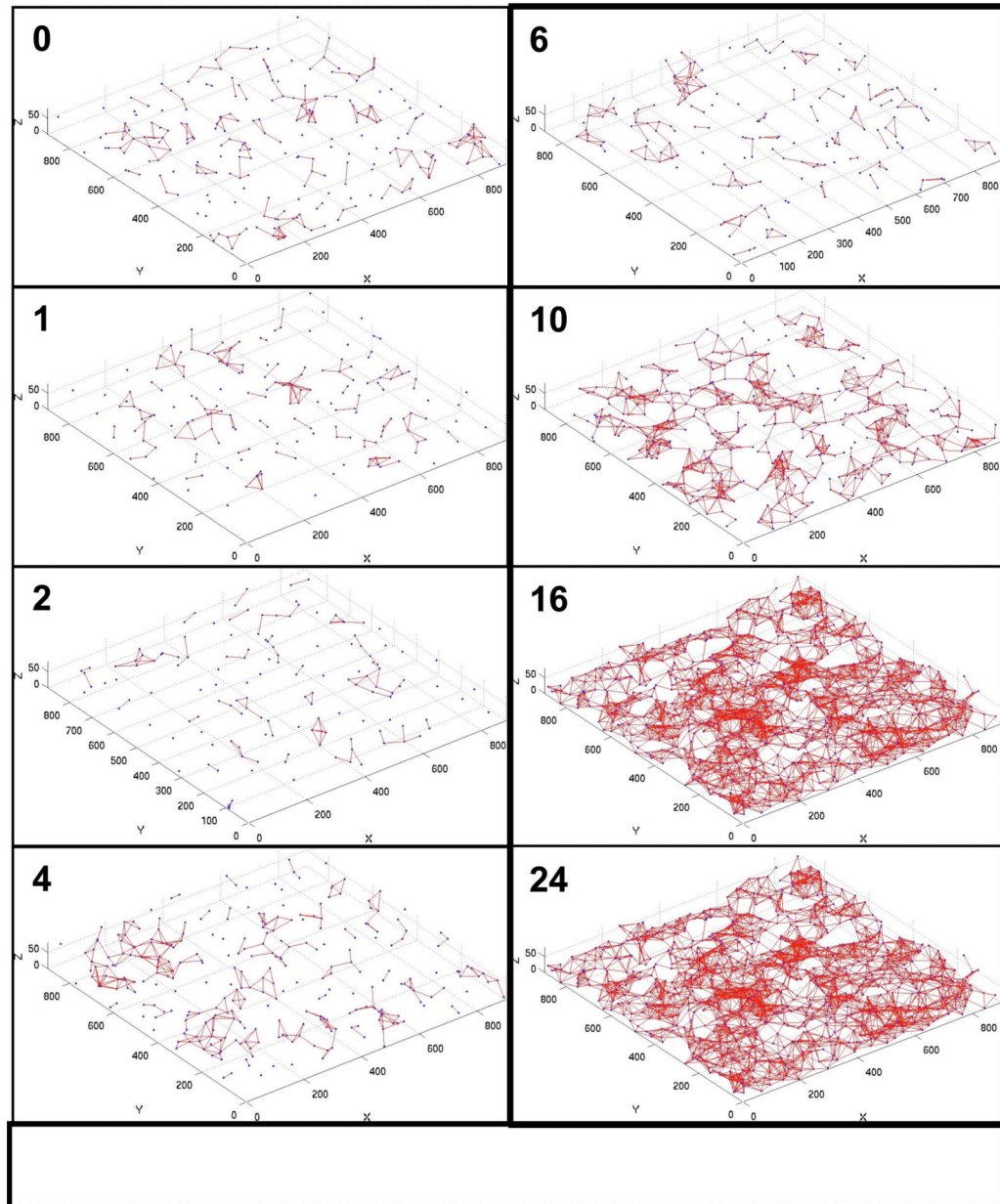
Figure 5.4.
Cell graphs produced from human MSC embedded in 3D collagen matrices. Graphs show nuclei and development of edges (relationships) between them over time [91]. There is a phase transition sometime between hour 10 and hour 16 and the graph becomes connected.
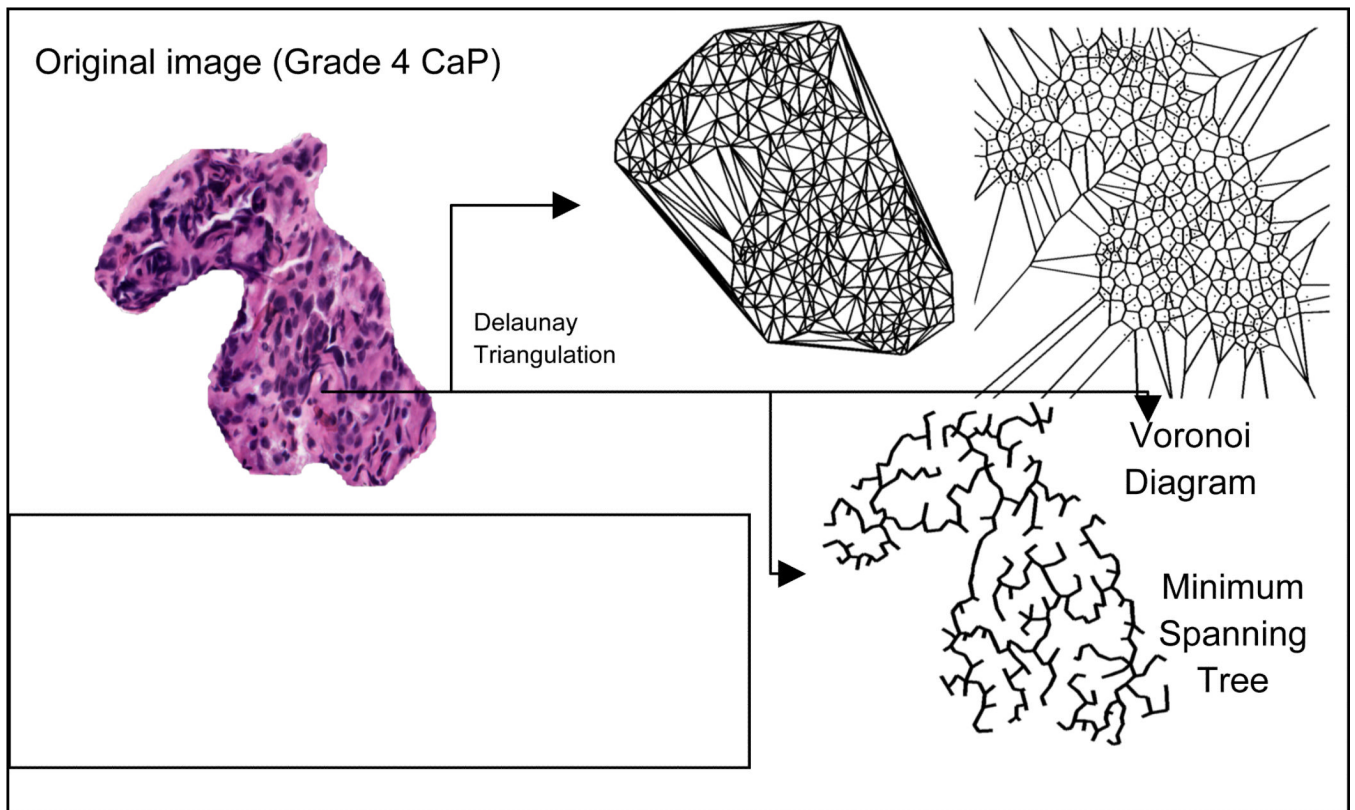
Figure 5.5.
(a) A digitized histopathology image of Grade 4 CaP and different graph based representations of tissue architecture via Delaunay Triangulation, Voronoi Diagram, and Minimum Spanning tree.
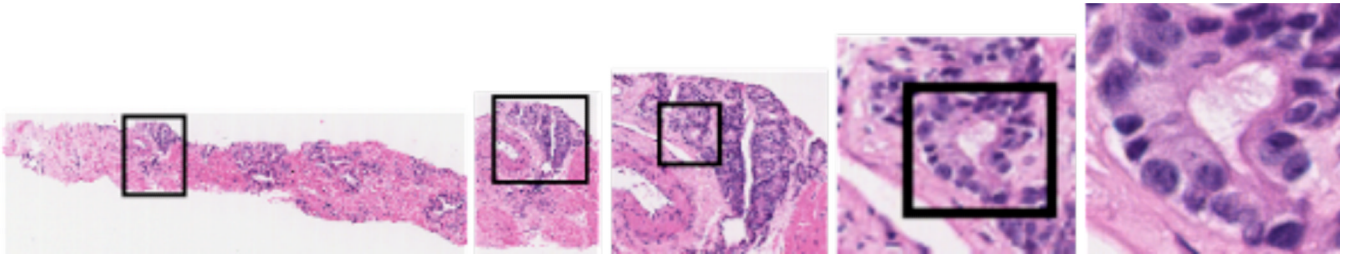
Figure 5.6.
Digitized histological image at successively higher scales (magnifications) yields
incrementally more discriminatory information in order to detect suspicious regions.

Figure 5.7.
Results from the hierarchical machine learning classifier. (a) Original image with the tumor region (ground truth) in black contour, (b) results at scale 1, (c) results at scale 2, and (d) results at scale 3. Note that only areas determined as suspicious at lower scales are considered for further analysis at higher scales.

(a) Low Grade (Yellow Triangles)

(b) High Grade (Red Triangles)
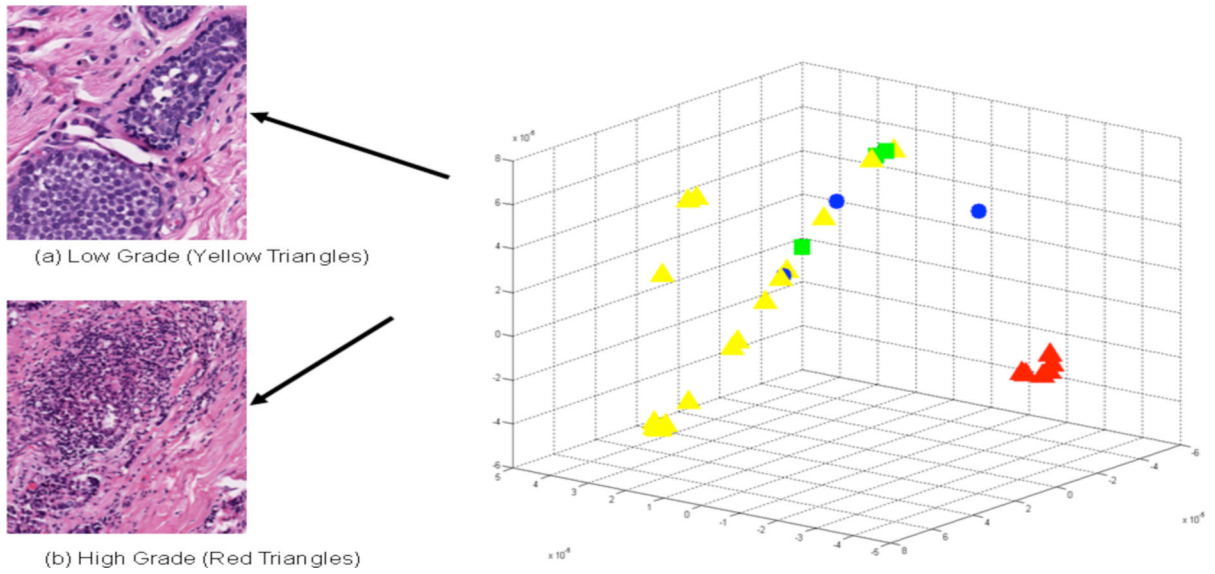
Figure 5.8.
Low dimensional embedding reveals innate structure in textural features of invasive breast cancers, with clear separation of high grade tumors from low and intermediate grade tumors as assessed by Nottingham score. Combined Nottingham score 5 (yellow triangle), 6 (green squares), 7 (blue circles), and 8 (red triangles). The score of 8 corresponds to high grade tumors.
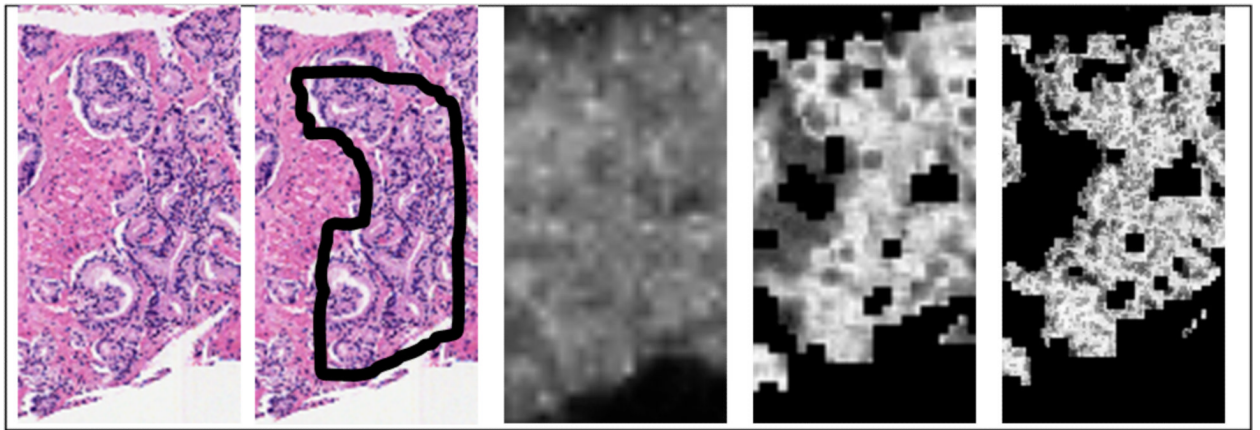
Figure 6.1.
From left to right, (a) A digitized histopathology image, (b) cancer extent delineated in black by an expert pathologist, and cancer probability images generated by an Adaboost classifier at (c) low-, (d) intermediate, and (e) high image resolutions.
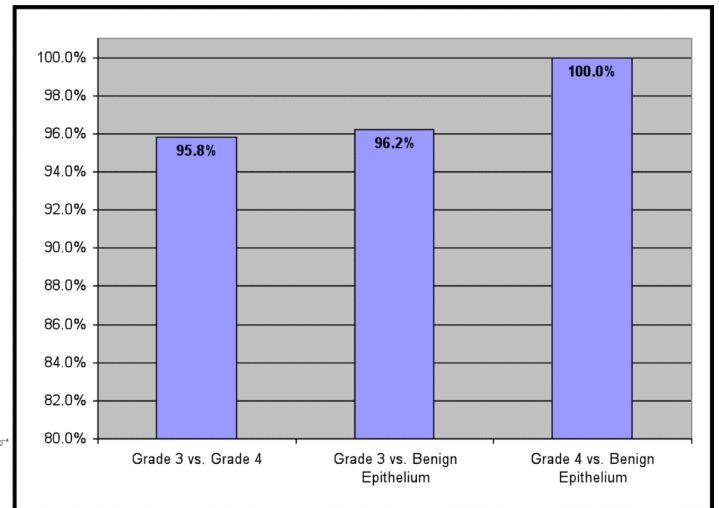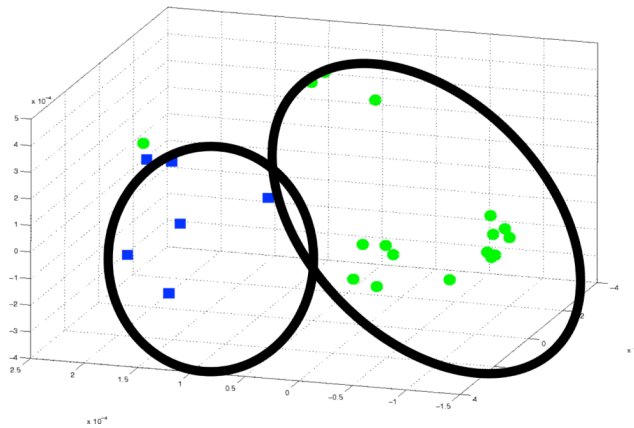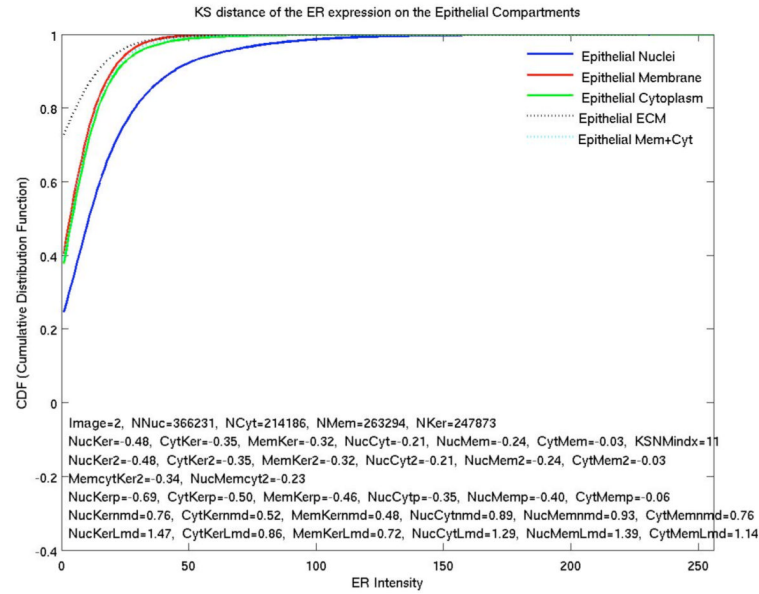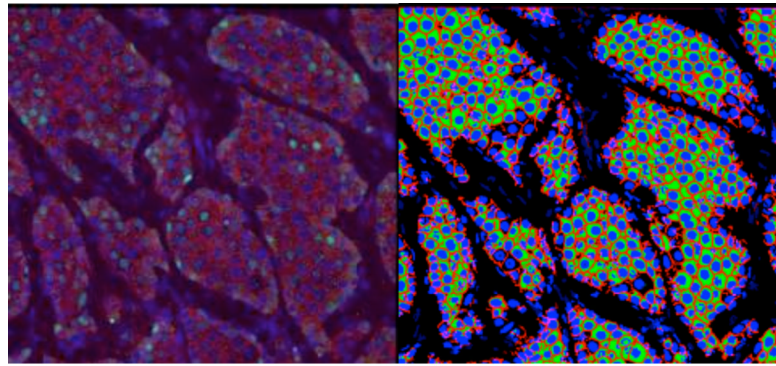
Figure 6.2.
(a) (left panel) Low dimensional representation (via non-linear dimensionality reduction) of prostate cancer histopathology images (green circles are Grade 3 images and blue squares represent Grade 4 prostate cancer images). A non-linear SVM is used to classify objects in the reduced dimensional space. (b) Right panel shows a classification accuracy of over 90% in distinguishing between Grade 3, Grade 4 images and comparable accuracy in distinguishing between benign stromal, epithelial and prostate cancer tissue.

Figure 6.3.
(**a**) A histological section stained with nuclear (DAPI-Blue), membrane (Pan-cadherin, red), and a target protein (Estrogen Receptor (ER), green). (**b**) Automatically segmented subcellular regions; membrane(red), nuclei(blue), cytoplasm(green). Dark colors show the non-epithelial regions. (**c**) CDF of the ER distributions (nuclei in blue, membrane in red and cytoplasm in green plots).
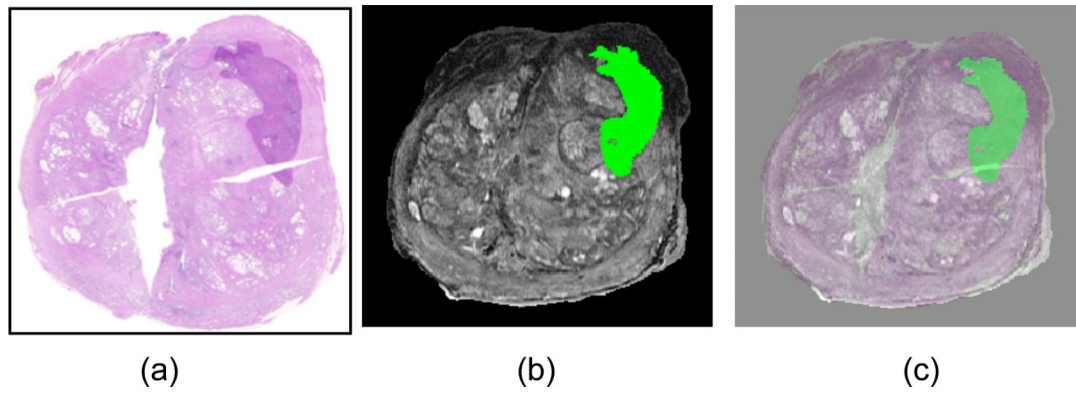
Figure 7.1.
(a) Histology section of prostate gland with CaP extent stained in purple (upper right) and corresponding mapping of CaP extent via COFEMI onto (b) MRI (CaP extent shown in green). (c) Overlay of histological and MRI prostate sections following registration.

Table 5.1

Summary of object-level features used in histopathology image analysis.

Category	Features
Size and Shape	Area
	Elliptical Features: Major and minor axis length, eccentricity, orientation, elliptical deviation
	Convex Hull Features: Convex area, convex deficiency, solidity
	Filled Image Features: Filled area, Euler number
	Bounding Box Features: Extent, aspect ratio
	Boundary Features: Perimeter, radii, perimeter Fourier energies, perimeter curvature, bending energy, perimeter fractal dimension
	Other Shape Features: Equivalent diameter, sphericity, compactness, inertia shape
	Center of Mass
	Reflection Symmetry
Radiometric and Densitometric	Image Bands, Intensity
	Optical density, integrated optical density, and mean optical
	Hue
Texture	Co-occurrence Matrix Features: Inertia, energy, entropy, homogeneity, maximum probability, cluster shade, cluster
	Fractal Dimension
	Run-length Features: Short runs emphasis, long runs emphasis, gray-level non-uniformity, run-length non-uniformity, runs percentage, low gray-level runs emphasis, high gray-level runs
	Wavelet Features: Energies of detail and low resolution images
	Entropy
Chromatin-Specific	Area, integrated optical density, mean optical density, number of regions, compactness, distance, center of mass

Table 5.2

Summary of spatial-arrangement features used in histopathology image analysis.

Graph Structure	Features
Voronoi Tesselation	Number of nodes, number of edges, cyclomatic number, number of triangles, number of k-walks, spectral radius, eigenexponent, Randic index, area, roundness factor, area disorder, roundness factor homogeneity
Delaunay Triangulation	Number of nodes, edge length, degree, number of edges, cyclomatic number, number of triangles, number of k-walks, spectral radius, eigenexponent, Wiener index, eccentricity, Randic index, fractal dimension
Minimum Spanning Tree	Number of nodes, edge length, degree, number of neighbors, Wiener index, eccentricity, Randic index, Balaban index, fractal dimension
O'Callaghan Neighborhood Graph	Number of nodes, number of edges, cyclomatic number, number of neighbors, number of triangles, number of k-walks, spectral radius, eigenexponent, Randic index, fractal dimension
Connected Graph	Number of nodes, edge length, number of triangles, number of k-walks, spectral radius, eigenexponent, Wiener index, eccentricity, Randic index, fractal dimension
Relative Neighbor Graph	Number of nodes, number of edges, cyclomatic number, number of neighbors, number of triangles, number of k-walks, spectral radius, eigenexponent, Randic index, fractal dimension
k-NN Graph	Number of nodes, edge length, degree, number of triangles, number of k-walks, spectral radius, eigenexponent, Wiener index, eccentricity, Randic index, fractal dimension

Table 6.1

the average accuracy results of the diseased-healthy-damaged classification on the test set by using five different approaches

Brain Tissue	Cell Graph	Cell Dist	Textural	Intensity	Voronoi
Overall	95.45 (±)1.33	84.34 (±)5.52	89.03 (±)1.51	62.50 (±)3.76	93.35 (±)0.47
Diseased	95.14 (±)2.03	80.66 (±)7.96	89.04 (±)2.01	62.27 (±)3.94	92.73 (±)0.27
Healthy	98.15 (±)0.00	98.15 (±)0.00	97.22 (±)1.44	91.60 (±)6.24	98.15 (±)0.00
Damaged	92.50 (±)1.76	64.38 (±)14.87	75.21 (±)4.56	14.58 (±)4.21	88.44 (±)3.09